University of Tartu
Faculty of Science and Technology
Institute of Physics

Kristjan Eimre

Multiscale electrical and thermal simulations of metal surface defects in high electric field

Master's thesis

Supervisor: PhD Vahur Zadin

Tartu 2017

Title

Multiscale electrical and thermal simulations of metal surface defects in high electric field

Author

Kristjan Eimre

Abstract

Vacuum electrical breakdowns disrupt the performance of many devices that use high magnitude electric fields. One of such devices is the Compact Linear Collider, a planned particle accelerator at CERN. Vacuum breakdown events are caused by surface defects on cathodes, which enhance the electric field locally, emit emission currents and as a result heat up until vaporization and plasma production. Understanding these processes is important for confining the frequency of vacuum breakdowns to satisfactory levels.

A comprehensive mathematical model for the electrical and thermal behaviour of surface defects was improved in this thesis by the addition of the Nottingham effect. A custom finite element software implementing this mathematical model was developed. Finite element calculations based on the mathematical model showed that the inclusion of the Nottingham effect reduced the melting fields of copper surface defects by up to 27%. Additionally, a collective effect of multiple emitters was found, which can arbitrarily change the estimated field enhancement factor obtained from Fowler-Nordheim plots.

To validate the work function variation in the finite element calculations, density functional theory (DFT) calculations of various atomic scale copper defects were conducted. With no applied electric field, the largest work function reduction with respect to clean (111) surface value of 4.84 eV was found to be 0.58 eV. Methodology for assessing work function from DFT potential landscapes with tight-binding quantum transport simulations was developed and applied to the studied defects. In the case of all defects, electric field further increased the reduction of work function with respect to the clean (111) surface and the largest reduction for the electric field of 4 GV/m was 1.31 eV.

Keywords

multiscale simulations, electron emission, Nottingham effect, work function

CERCS code

P260 (Condensed matter: electronic structure, electrical, magnetic and optical properties, superconductors, magnetic resonance, relaxation, spectroscopy)

Pealkiri

Kõrges elektriväljas metalli pinnadefektide elektriline ja termiline multiskaala simuleerimine

Autor

Kristjan Eimre

Lühikokkuvõte

Elektriliste vaakumläbilöökide esinemine piirab mitmete kõrgeid elektrivälju kasutavate seadmete tööd. Üks selline seade on Euroopa Tuumauuringute Keskuse (CERN) poolt plaanitav Kompaktne Lineaarpõrguti (CLIC). Vaakumläbilöökide põhjuseks on katoodide peal esinevad pinnadefektid, mis võimendavad lokaalselt elektrivälja, emiteerivad emissioonivoolu ja selle tulemusel kuumenevad kuni aurustumiseni. Vaakumläbilöökide sageduse piiramiseks alla rahuldava taseme on oluline eelnevalt mainitud protsesside detailne mõistmine.

Käesolevas töös lisati Nottinghami efekt pinnadefektide elektrilise ja termilise käitumise matemaatilisele mudelile. Lisaks loodi antud matemaatilise mudeli põhjal lõplike elementide analüüsi tarkvara. Lõplike elementide simulatsioonide tulemused näitasid, et Nottinghami efekti lisamine vähendas vase pinnadefektide sulamiseks vajalikke elektrivälju kuni 27%. Lisaks leiti, et mitmete pinnadefektide koosmõju võib meelevaldselt muuta Fowler-Nordheimi sõltuvusest hinnatud väljavõimendustegurit.

Lõplike elementide simulatsioonides varieeriti pinnadefektide väljumistööd. Selle valideerimiseks viidi läbi erinevate atomistlike vase pinnadefektide tihedusfunktsionaali teooria arvutusi. Sileda vase (111) pinna väljumistöö väärtuseks saadi 4.84 eV. Sellega võrreldes vähenes defektsete pindade puhul väljumistöö kuni 0.58 eV võrra. Lisaks arendati välja metoodika, mis lubab elektrivälja puhul hinnata pinnadefektide väljumistöid. See metoodika põhineb lisaks tihedusfunktsionaali teooria arvutustele ka kvant-transpordi simulatsioonidel. Seda rakendati uuritud vase atomistlike pinnadefektide puhul. Elektrivälja 4 GV/m puhul vähenes kõige rohkem väljumistöö 1.31 eV võrra, sileda (111) pinnaga võrreldes.

Märksõnad

multiskaala simulatsioonid, eletronide emissioon, Nottinghami efekt, väljumistöö

CERCS kood

P260 (Tahke aine: elektrooniline struktuur, elektrilised, magneetilised ja optilised omadused, ülijuhtivus, magnetresonants, spektroskoopia)

Contents

1 Introduction

1.1 Motivation

The European Organization for Nuclear Research (CERN) is investigating the feasibility of the Compact Linear Collider (CLIC), a TeV–range electron–positron collider [1, 2]. The particles are accelerated in copper structures by 12 GHz radio frequency electric field. The operating accelerating electric field is 100 MV/m, which, due to geometry of the accelerating structure, results in a peak surface electric field of approximately 250 MV/m [1, 3]. The main limiting factor to the performance of CLIC is the occurrence of vacuum breakdown events, which are caused by the high-magnitude electric field [4]. Vacuum breakdowns occur in the CLIC ultra high vacuum accelerating cavities during the accelerating electric field pulses and cause a large amount of energy to be released in the system. As a result, the accelerated particle bunches are deflected from their trajectories and lost. Understanding the origins of the vacuum electrical breakdowns is important for confining them to the desired level.

The classical vacuum electrical breakdown scenario [5, 6] is shown in Figure 1.1. The breakdown is initiated by a local defect, such as a protrusion, dust particle, scratch or something else, which causes the electric field to be locally significantly enhanced. This triggers electron emission currents from the defect. The defect in this context is called an emitter. Emission currents heat the emitter due to Joule heating and the Nottingham effect [7] until it vaporizes and produces a plasma cloud in the vacuum. According to several studies [8, 9], most of the heat generated due electron emission is provided by the Nottingham effect, making it critical for accurate estimation of the thermal behaviour. The conductive plasma in the vacuum, created from the vaporization of multiple field emitters, causes the large current spike [10] and disrupts the accelerated particles. In the aftermath, a crater and other surface defects are left behind, possibly becoming new field emitters. Figure 1.2 shows a scanning electron microscope image of a copper cathode after a vacuum breakdown event.

Experimental investigations in direct current (DC) conditions have shown that the copper cathodes used in the CLIC accelerating cavities have a microscopic electric field enhancement in the range of $\beta = 30$ to 140 [11, 12]. This would correspond to very sharp protrusions on the cathode, as the local field enhancement of a protrusion is roughly equal to its height and radius ratio. These sharp protrusion have not been observed. The high field enhancement value is obtained by measuring the slope of Fowler-Nordheim plots, see Figure 1.3 for an example. This analysis assumes ideal Fowler-Nordheim conditions [13, 14], which disregard elevated temperatures in the emitters. Additionally, the analysis assumes that the cathode has static field emitters, which provide a constant field enhancement during the ramping up of the electrical field until breakdown occurs. Therefore, it is instructive to investigate the collective effects of multiple emitters, especially when some of them start to melt and vaporize.

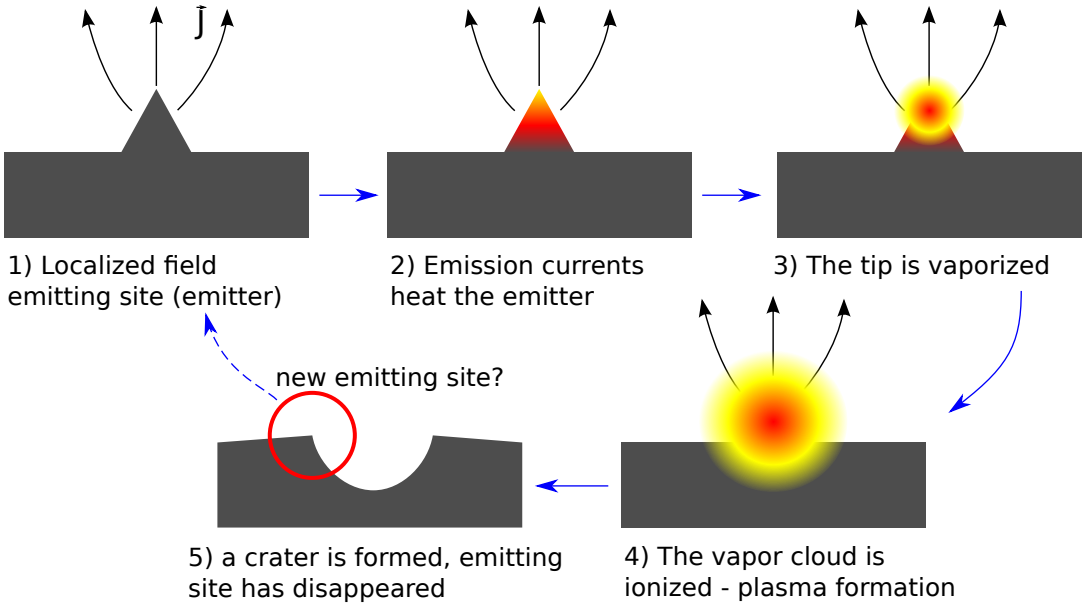

Figure 1.1: The classical breakdown mechanism. 1) The cathode surface contains small localized current emitting sites (protrusions, dust particles, scratches, etc). 2)–4) Emission currents heat the emitter until it vaporizes and produces a plasma cloud. 5) A crater with possibly sharp edges remains, which can act as a new emitting site. Wide damaged areas on the cathode after a breakdown event are thought to be caused by a large number of these vaporizations.

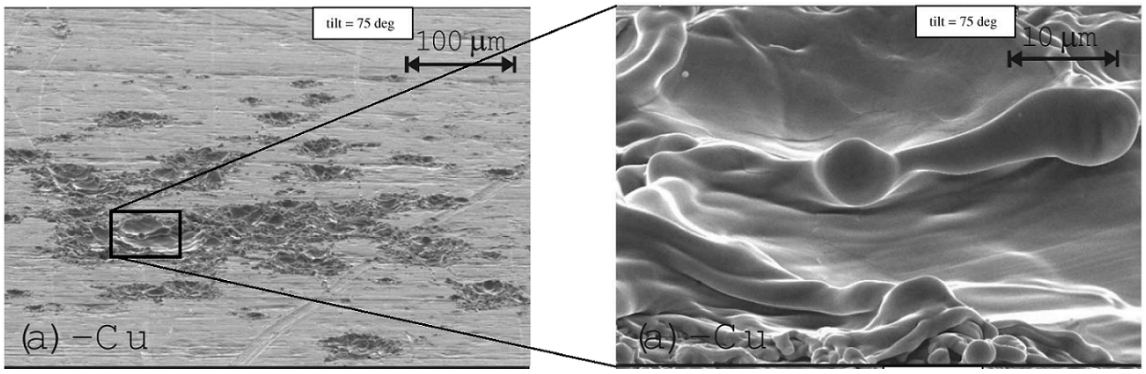

Figure 1.2: Scanning electron microscope pictures of the aftermath of a vacuum breakdown event in DC conditions. Microscopic defects are shown, where the electric field is locally enhanced and work function is possibly lowered. Figure adapted from [4].

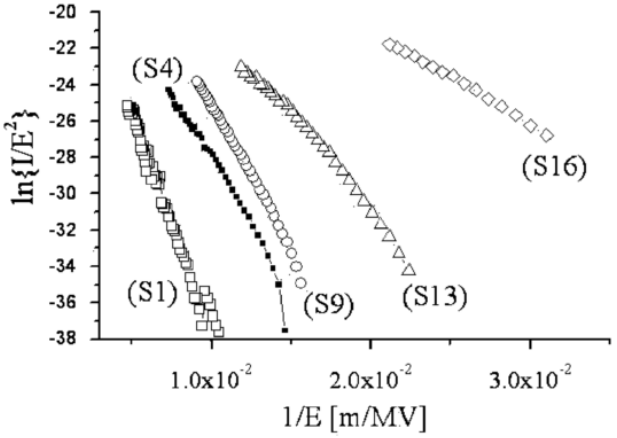

Figure 1.3: Fowler-Nordheim plots of vacuum breakdown experiments in DC conditions conducted by Kildemo et al. I is the total measured current and E is the macroscopic electric field at the surface of the cathode. The field enhancement factor is found by $\beta = -(62.3\,\mathrm{GV/m})/\gamma$, where γ is the slope of the FN plot and work function of 4.5 eV is assumed. See Section 2.3 for the derivation of this relation. The obtained β values for the curves are the following S1: 102, S4: 150, S9: 114, S13: 94 and S16: 45. Figure taken from [12].

Field emission current and the resulting heating depend strongly on the local work function of the surface. Experiments have shown that the local work function near atomic scale surface defects can be considerably reduced with respect to the clean surface [15, 16]. The field enhancement estimation from Fowler-Nordheim plots is usually done by assuming a constant copper work function of $\phi = 4.5\,\mathrm{eV}$. If the value of the work function is lower than this in reality, then so is the real field enhancement factor. This provides a possible explanation to the high field enhancement estimations obtained from experiments. Density functional theory calculations have shown that the work function near single adatoms can be reduced considerably [17]. However, on real cathodes much more complicated surface defects can exist. Additionally, the local work function can potentially depend on the electric field. Therefore it is important to investigate how exactly different kinds of surface defects affect the local work function value. An accurate local work function determination method near surface defects has a much wider range of applications than just in the study of vacuum breakdown initiation.

1.2 The objective of this work

The main objective of this work was to improve the mathematical model describing the electrical and thermal behaviour of metal surface defects by including the Nottingham effect, assess its influence to the thermal behaviour and to use the model to investigate possible collective effects of multiple emitters on the Fowler-Nordheim plot. In order to do this, multiple different surface defects with different work functions were studied. To validate the variations in the work functions, density functional theory calculations were performed on atomic scale defects. Methodology was developed to assess the local work function dependence on the electric field and it was applied to the studied atomic scale defects. This is summarised in the block diagram in Figure 1.4. Additionally, a high performance finite element code based on the electrical and thermal model needed to be

developed. The main objective can be expressed as more specific sub-objectives:

- Include Nottingham effect in the surface defect mathematical model and assess its influence for systems with varying geometries and work functions with the finite element analysis.
- Investigate the collective behaviour of multiple different emitters and possible effects on the Fowler-Nordheim plot with the finite element analysis.
- Develop a high-performance finite element analysis code in C++ programming language based on the mathematical model of the electrical and thermal behaviour of surface defects.
- Perform density functional theory calculations to investigate the work function changes near atomic scale surface defects.
- Develop methodology for assessing the work function in cases with applied electric field with density functional theory and quantum transport calculation methods. Apply this methodology for the studied atomic scale surface defects.

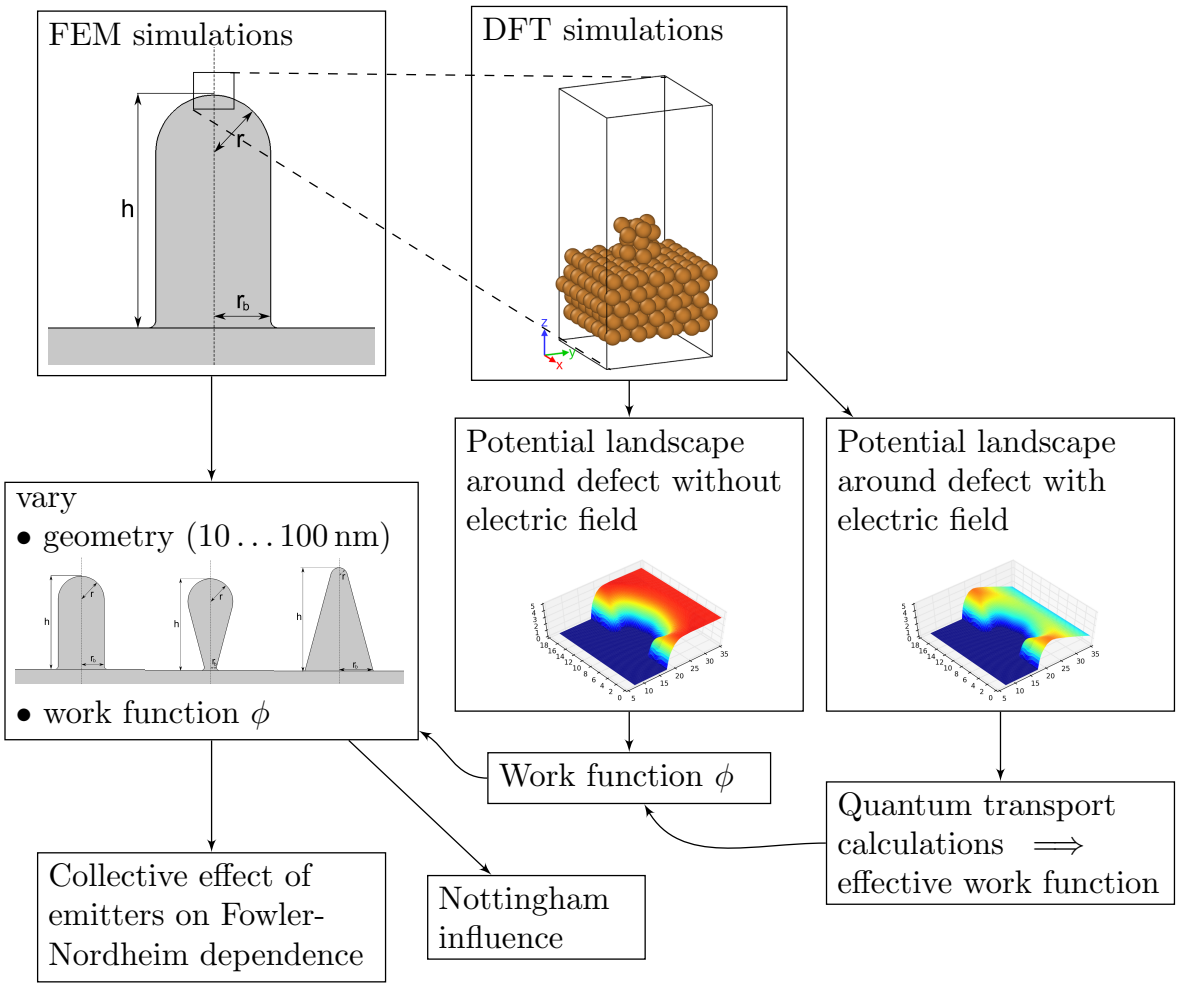

Figure 1.4: Overview of the methodology and objectives of the work.

1.3 Author's contribution

The mathematical model for electrical and thermal behaviour of surface defects was originally put together by Vahur Zadin and was improved by the author's bachelor's work. During the work this thesis, the mathematical model was improved by the addition of Nottingham effect and by accurate calculation of emission currents directly from the definition integral. The finite element implementation in COMSOL and all of the simulations and analysis were the author's contribution. The custom C++ code based on the mathematical model was also developed solely by the author.

Most of the density functional theory calculations were ran by Artur Tamm. The small part of the calculations ran by the author was also guided by Artur Tamm. The analysis of the results of the density functional theory calculations was done by the author. The methodology to calculate the work function via tight binding quantum transport method was developed and the simulations were ran solely by the author.

2 Theoretical overview

2.1 Electron emission

2.1.1 Free electron model

The free electron theory [18, 19] has provided the basis for most of the quantum-mechanical theories of electron emission from metals, including the widely used Fowler-Nordheim emission equation.

The free electron theory assumes that conduction electrons in metals do not interact with each other nor with the periodic crystal lattice. The electrons behave effectively as if they were particles in a box of dimensions L^3. Periodic boundary conditions are imposed on the edges of the crystal. The solution of the corresponding Schrödinger equation provides the wave functions $\Psi_{\boldsymbol{k}}$ and corresponding energies $E_{\boldsymbol{k}}$, given by

$$\Psi_{\boldsymbol{k}}(\boldsymbol{r}) = \frac{1}{L^{3/2}} \exp(i\boldsymbol{k}\cdot\boldsymbol{r}), \tag{2.1}$$

$$E_{\boldsymbol{k}} = \frac{\hbar^2 k^2}{2m}, \tag{2.2}$$

$$\boldsymbol{k} = \frac{2\pi}{L}(n_x, n_y, n_z), \quad n_{x,y,z} = 0, \pm 1, \pm 2, \ldots \tag{2.3}$$

where $\boldsymbol{k}$ is the wave vector and its discretization originates from the periodic Born-von Karman boundary conditions. Additionally, $\hbar$ is the reduced Planck's constant, $k = |\boldsymbol{k}|$ and m is the effective electron mass.

Considering that in k space, the distance between two points is $2\pi/L$, then the number of possible states in volume $V = L^3$, taking spin into account, with energies from 0 to E is

$$N_{\text{states}}(E) = \frac{2}{(2\pi/L)^3}\int d\boldsymbol{k} = \frac{2}{(2\pi/L)^3} 4\pi \int_0^{\sqrt{\frac{2mE}{\hbar^2}}} k^2 dk = \frac{V}{3\pi^2}\left(\frac{2mE}{\hbar^2}\right)^{3/2} \tag{2.4}$$

The density of states, or the number of electron states per unit volume with energy between E and $E + dE$, is given by

$$\rho(E) = \frac{1}{V}\frac{dN_{\text{states}}(E)}{dE} = \frac{1}{2\pi^2}\left(\frac{2m}{\hbar^2}\right)^{3/2} E^{1/2}. \tag{2.5}$$

For a system in thermodynamic equilibrium, the probability of an electron state with energy E being occupied is given by the Fermi-Dirac distribution function

$$f_{\text{FD}}(E) = \frac{1}{1 + \exp\left(\frac{E-\mu}{k_B T}\right)}, \tag{2.6}$$

where k_B is Boltzmann's constant, T is the absolute temperature, and μ is the chemical potential.

To describe electron emission, an expression is required for the number of electrons which cross a unit area (without losing generality, the area is assumed to be normal to x direction), per unit time, with total energy between E and $E + dE$ and normal energy defined by $E_x = \frac{\hbar^2 k_x^2}{2m}$ between E_x and $E_x + dE_x$. Denoting this quantity by $N(E, E_x)dEdE_x$, we have

$$N(E, E_x)dEdE_x = \frac{2f_{\mathrm{FD}}(E)}{(2\pi)^3} \int\limits_{(E,E_x)} v_x d\boldsymbol{k}, \tag{2.7}$$

where

$$v_x = \sqrt{\frac{2E_x}{m}} = \frac{\hbar k_x}{m} \tag{2.8}$$

is the velocity of the electron normal to the unit area under consideration, and (E, E_x) indicates that only states with total energy between E and $E + dE$ and normal energy between $E_x + dE_x$ are included in the integration. It can be shown (see appendix A) that

$$N(E, E_x)dEdE_x = \frac{m}{2\pi^2\hbar^3} f_{\mathrm{FD}}(E)dEdE_x. \tag{2.9}$$

The number of electrons with the normal energy between E_x and $E_x + dE_x$ can be found by integrating over all possible total energy values E

$$N(E_x, T)dE_x = \frac{m}{2\pi^2\hbar^3} dE_x \int\limits_{E_x}^{\infty} f_{\mathrm{FD}}(E)dE = \frac{mk_BT}{2\pi^2\hbar^3} \ln\left[1 + \exp\left(-\frac{E_x - \mu}{k_BT}\right)\right] dE_x. \tag{2.10}$$

This result is known as the supply function and will be used in deriving the emission current density equations later on. Figure 2.1 shows the dependence of the supply function on electron energies for copper.

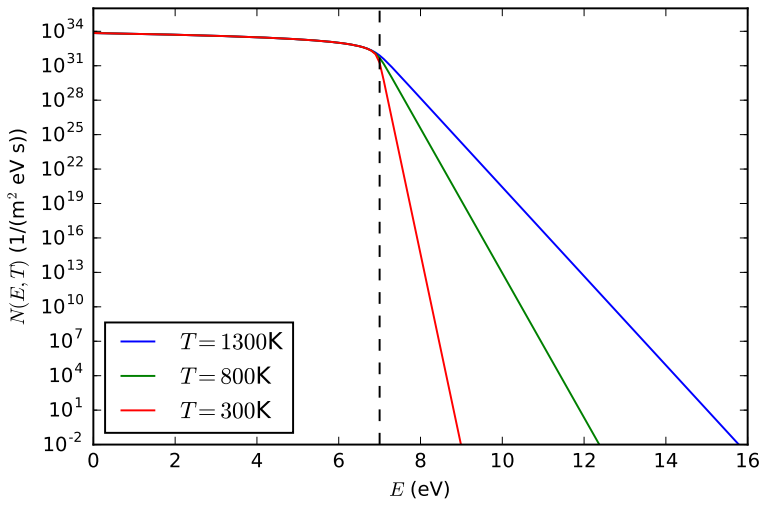

Figure 2.1: The supply function dependence on the electron energies for three temperatures. The chemical potential is $\mu = 7\,\mathrm{eV}$ (copper).

2.1.2 Metal surface barrier

Conduction electrons reaching the metal surface must overcome a potential barrier to escape the metal. For electrons with Fermi energy[1], the minimal additional energy needed to escape is the work function ϕ. After leaving the metal surface, an electron is attracted back to the metal by the image force (resulting potential is $-\frac{e^2}{16\pi\varepsilon_0 x}$, where e is the elementary charge, ε_0 is the electric constant and x is the distance from the metal surface). This arises from quantum mechanical exchange-correlation effects. Additionally, when an electric field F is applied on the metal surface, the potential is modified further by $-eFx$. The resulting potential is

$$V(x) = E_F + \phi - eFx - \frac{e^2}{16\pi\varepsilon_0 x} \tag{2.11}$$

and is known as the Schottky-Nordheim barrier [19–21]. In Figure 2.11, the potential is shown for two different electric fields. The peak of the barrier depends also on the field (this is known as the Schottky effect) and is given by

$$V_{\max} = E_F + \phi - \sqrt{\frac{e^3 F}{4\pi\varepsilon_0}}. \tag{2.12}$$

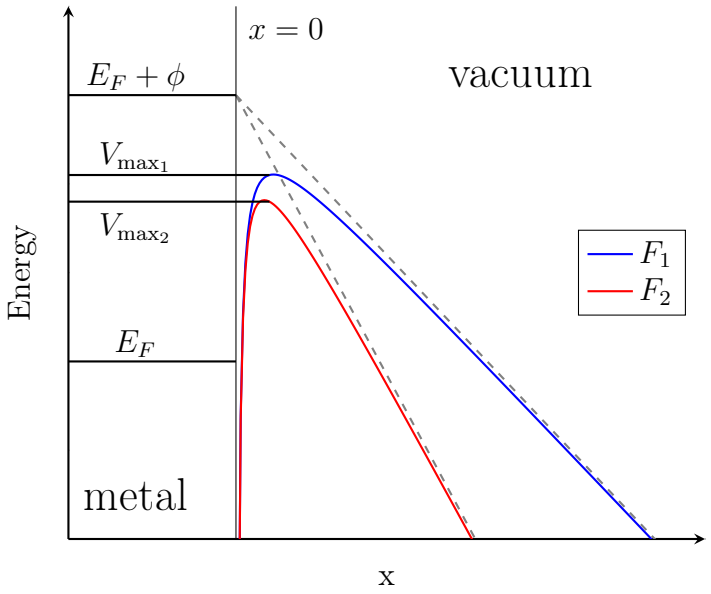

Figure 2.2: Schottky-Nordheim barrier for two different electric fields F_1 and F_2, whereas $F_2 > F_1$. Metal-vacuum boundary is located at $x = 0$. For the dashed lines, the image charge potential is ignored and they correspond to the triangular barriers.

The Schottky-Nordheim barrier is an approximation that is widely used and is the basis for most analytical emission current equations, but it tends to underestimate the real surface barrier by a small margin. The simpler analytical barrier is the triangular barrier $V_{\text{tria}}(x) = E_F + \phi - eFx$, which disregards the image force effect. The real potential barrier is known to be between these two analytical approximations [22]. In the results chapter of this work, the barriers from density functional theory calculations are shown.

[1]In this work, no distinction is made between the chemical potential and the Fermi level and they are assumed to be the same $E_F = \mu$.

2.1.3 Transmission probability

The probability for an electron to surpass the Schottky-Nordheim barrier (2.11) depends on its energy and can be calculated by numerically solving the corresponding Schrödinger equation [19, 20] or by employing the Wentzel-Kramers-Brillouin (WKB) approximation [23]. These approaches include numerical evaluations and are accurate, but they do not lead to analytical expressions and thus are not appropriate for general analysis of electron emission. A better method in this regard has been developed by Miller and Good [24] and has been extensively used in the study of electron emission. Their method is a generalization of the ordinary WKB method and it leads to the WKB results under certain limiting conditions. It is applicable to a potential barrier with only two classical turning points (such as the Schottky-Nordheim barrier) and the transmission coefficient $D(E,F)$ is given by the following expression

$$D(E,F) = (1+\exp[Q(E,F)])^{-1}, \tag{2.13}$$

$$Q(E,F) = -2i\int_{x_1}^{x_2}\sqrt{\frac{2m}{\hbar^2}[E-V(x,F)]}dx, \tag{2.14}$$

where E is the electron energy normal to the surface and it may be above or below the top of the barrier and $x_{1,2}$ are the points were the integrand is zero (they are complex when E is above the barrier maximum). Equation (2.14) is not applicable when energies are high enough to cause $\mathrm{Re}(x)\to 0$ (singularity in the image force part), this sets following limit

$$E < E_l \equiv V_{\max} + \left(1-\frac{1}{\sqrt{2}}\right)\sqrt{\frac{e^3F}{4\pi\varepsilon_0}}. \tag{2.15}$$

For energies higher than E_l, however, the transmission probability can be taken to be unity. For $E<E_l$, the calculation of $D(E,F)$ can be expressed in the following form [14]

$$Q(E) = \frac{4}{3}\frac{1}{\hbar eF}\sqrt{2m|\phi+E_F-E|^3}\nu(y), \tag{2.16}$$

$$y(E) = \sqrt{\frac{e^3F}{4\pi\varepsilon_0}}\frac{1}{|\phi+E_F-E|}, \tag{2.17}$$

$$\nu(y) = \begin{cases} -\sqrt{\frac{y}{2}}\left\{-2E_\theta\left[\sqrt{\frac{y-1}{2y}}\right]+(y+1)K_\theta\left[\sqrt{\frac{y-1}{2y}}\right]\right\}, & \text{for } y>1, \\ \sqrt{1+y}\left\{E_\theta\left[\sqrt{\frac{1-y}{1+y}}\right]+yK_\theta\left[\sqrt{\frac{1-y}{1+y}}\right]\right\}, & \text{for } y<1, \end{cases} \tag{2.18}$$

where $E_\theta[k]$ and $K_\theta[k]$ are the well-known elliptic integrals

$$K_\theta[k] = \int_0^{\pi/2}\frac{d\theta}{(1-k^2\sin^2\theta)^{1/2}}, \tag{2.19}$$

$$E_\theta[k] = \int_0^{\pi/2}(1-k^2\sin^2\theta)^{1/2}d\theta. \tag{2.20}$$

For the elliptic function $\nu(y)$, Forbes [25] has introduced the following very simple and widely used analytical approximation accurate to 0.33% for $0\leqslant y\leqslant 1$

$$\nu(y) = 1-y^2+\frac{1}{3}y^2\ln(y). \tag{2.21}$$

Now, the transmission probability $D(E, F)$ can be evaluated analytically and it is shown on Figure 2.3 for copper parameters ($E_F = 7.0\,\text{eV}$, $\phi = 4.5\,\text{eV}$) and for three different field values.

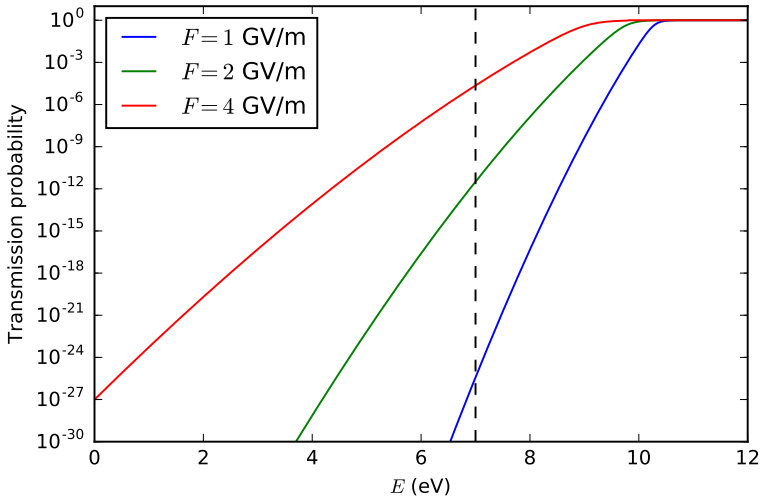

Figure 2.3: Transmission probability $D(E, F)$ for copper parameters ($E_F = 7.0\,\text{eV}$, $\phi = 4.5\,\text{eV}$) and three different electric fields.

2.1.4 Emission current

The number of electrons reaching the metal surface per unit area per unit time with normal energy between E and $E + dE$ is given by the supply function $N(E, T)$ (2.10). Each of these electrons has a probability of $D(E, F)$ (2.13) to be transmitted through the surface potential barrier. Hence, the emitted current density is [7, 19, 20, 26, 27]

$$J(F, T) = e \int_0^\infty N(E, T) D(E, F) dE. \tag{2.22}$$

Substituting the supply function (2.10) and the transmission probability (2.13) into the emission current equation (2.22), we obtain

$$J(F, T) = \frac{emk_BT}{2\pi^2\hbar^3} \left\{ \int_0^{E_l} \frac{\ln(1 + \exp[-(E - E_F)/k_BT])dE}{1 + \exp(Q(E, F))} + \int_{E_l}^\infty \ln(1 + \exp[-(E - E_F)/k_BT])dE \right\}. \tag{2.23}$$

Equation (2.23) can be directly integrated and the result is shown in Figure 2.4 as a function of applied field for three different temperature values. As can be seen, each of the curves has two distinct regions (except for the $T = 300\,\text{K}$ curve, which goes out of the plot limits at lower fields). At lower fields, the field dependence of the emission current is weaker than at higher fields. This region is called the thermionic emission regime and the main mechanism of emission is by thermally excited electrons surpassing the barrier

above the barrier maximum. At higher fields, the field dependence is stronger and this is called the field emission regime. The main mechanism of emission in this regime is electron tunnelling through the potential barrier.

Under certain temperature and field conditions, e.g. the previously described field emission or thermionic emission conditions, the integral in equation (2.23) can evaluated analytically.

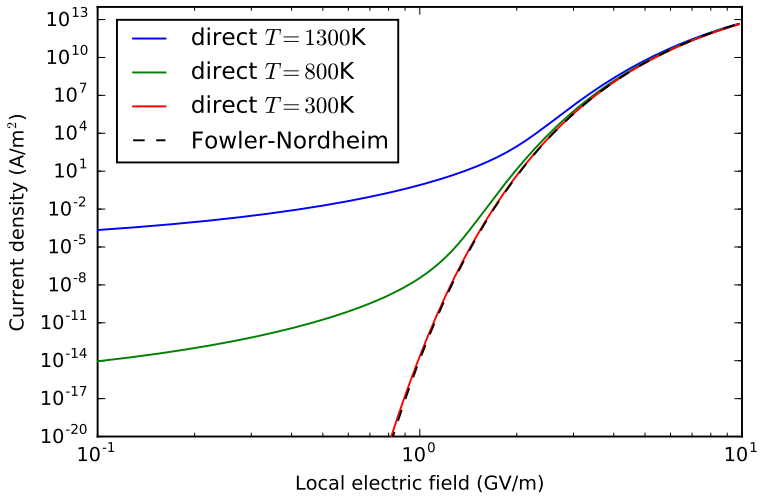

Figure 2.4: Eq. (2.22) directly integrated as a function of electric field for three different temperatures and the Fowler-Nordheim (2.33) equation. Copper conditions of $\phi = 4.5\,\mathrm{eV}$ and $E_\mathrm{F} = 7\,\mathrm{eV}$ were assumed.

2.1.5 Fowler-Nordheim equation

It can be seen from Fig. 2.1, that for sufficiently low temperatures, $N(E,T)$ diminishes rapidly for $E > E_F$. On the other hand, the transmission probability $D(E,F)$ diminishes rapidly for $E < E_F$. Under these conditions, the second integral in (2.23) is negligible and the integrand in the first integral vanishes except in the immediate neighbourhood of the Fermi level. The limits of the first integral can be chosen as $-\infty$ and ∞. Also, under these conditions

$$\exp[Q(E)] \gg 1. \tag{2.24}$$

Considering all of this, the integral in (2.23) can be simplified to [19, 20]

$$J(F,T) = \frac{emk_BT}{2\pi^2\hbar^3} \int_{-\infty}^{\infty} \exp[-Q(E)] \ln\left[1 + \exp\left(-\frac{E - E_F}{k_BT}\right)\right] dE. \tag{2.25}$$

Since most of the contribution to the above integral comes from around Fermi level, the transmission coefficient exponent may be replaced by two terms of its Taylor expansion around Fermi level

$$-Q(E) \approx -b_0 + c_0(E - E_F), \tag{2.26}$$

where

$$b_0 \equiv \frac{4}{3}\sqrt{\frac{2m}{\hbar^2}}\frac{\phi^{3/2}}{eF}\nu(y_0), \tag{2.27}$$

$$c_0 \equiv 2\sqrt{\frac{2m}{\hbar^2}}\frac{\phi^{1/2}}{eF}\tau(y_0), \tag{2.28}$$

$$\tau(y) \equiv \nu(y) - \frac{2}{3}y\frac{d\nu}{dy} \approx 1 + \frac{1}{9}y^2[1 - \ln(y)], \tag{2.29}$$

$$y_0 \equiv y(E_F) = \sqrt{\frac{e^3F}{4\pi\varepsilon_0}}\frac{1}{\phi}. \tag{2.30}$$

Forbes' [25] approximation is used for $\tau(y)$ in (2.29). Now the integral in (2.25) can be evaluated

$$J(F,T) = \frac{emk_BT}{2\pi^2\hbar^3}\exp(-b_0)\int_{-\infty}^{\infty}\exp[c_0(E-E_F)]\ln\left[1+\exp\left(-\frac{E-E_F}{k_BT}\right)\right]dE \tag{2.31}$$

$$= \frac{e^3F^2}{16\pi^2\hbar\phi\tau^2(y_0)}\frac{\pi c_0k_BT}{\sin(\pi c_0k_BT)}\exp\left(-\frac{4}{3e}\sqrt{\frac{2m}{\hbar^2}}\nu(y_0)\frac{\phi^{3/2}}{F}\right). \tag{2.32}$$

At very low temperatures (when $\pi c_0 k_B T \ll 1$), (2.32) reduces to the well-known Fowler-Nordheim equation [13, 28]

$$J(F) = \frac{aF^2}{\phi\tau^2(y_0)}\exp\left(-\nu(y_0)\frac{b\phi^{3/2}}{F}\right), \tag{2.33}$$

where $y_0(F)$ is given by (2.30) and

$$a = \frac{e^3}{16\pi^2\hbar}, \tag{2.34}$$

$$b = \frac{4}{3e}\left(\frac{2m}{\hbar^2}\right)^{1/2} \tag{2.35}$$

are the first and second Fowler-Nordheim constant. The functions ν and τ are also called the Schottky-Nordheim barrier correction factors and would be both unity if the triangular barrier was assumed.

Figure 2.4 also shows the Fowler-Nordheim current. As seen, it matches well with the direct integration result for high field and low temperature conditions.

2.1.6 Nottingham effect

As electrons are emitted from the cathode, they are replaced at the surface by electrons with energy approximately equal to the Fermi energy to restore equilibrium conditions. This results in a heat flux on the surface, when the energy of the emitted electrons differs from Fermi energy. This phenomenon is called the Nottingham effect [7, 8, 29]. The cathode is heated if the average energy of the emitted electrons is below the Fermi energy, which corresponds to field emission conditions. The cathode is cooled if the average energy is above the Fermi energy, which corresponds to intermediate and thermionic emission conditions. Figure 2.5 illustrates these concepts.

The Nottingham heat flux is found by

$$\begin{aligned} q_{\mathrm{N}}(F,T,\phi) &= \int_0^\infty (E-\mu)\left(\frac{m}{2\pi^2\hbar^3} f_{\mathrm{FD}}(E,T)\right)\int_0^E D(E_x,F,\phi)dE_x dE \\ &= \frac{m}{2\pi^2\hbar^3}\int_0^\infty \frac{E-\mu}{1+\exp\left(\frac{E-\mu}{k_B T}\right)}\int_0^E D(E_x,F,\phi)dE_x dE, \end{aligned} \tag{2.36}$$

where $\left(\frac{m}{2\pi^2\hbar^3} f_{\mathrm{FD}}(E)\right)$ is the supply function corresponding to the total energy distribution of electrons given by (2.9) and $\int_0^E D(E_x,F,\phi)dE_x$ integrates the transmission probability over all electrons with normal energies E_x for a given total energy E. The average emitted electron energy difference from Fermi energy is given by

$$\langle \Delta E \rangle = \frac{q_N(F,T,\phi)}{\frac{1}{e}J(F,T,\phi)}, \tag{2.37}$$

where $J(F,T,\phi)$ is the emission current given by (2.22).

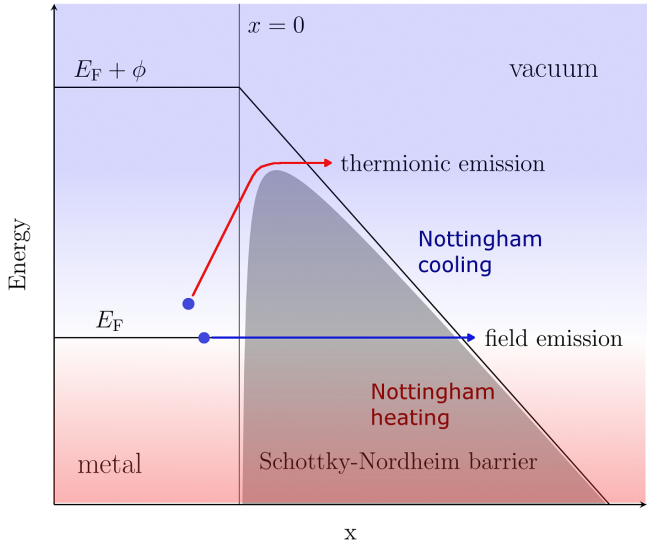

Figure 2.5: Possible electron emission mechanisms through the Schottky-Nordheim barrier and corresponding Nottingham heat flux. If electrons escape the metal under the Fermi level, the surface is heated and if the emitted electrons have higher energy than Fermi energy, the surface is cooled.

2.2 Work function

Work function is defined as the minimum amount of energy needed to extract an electron from the Fermi level of a metal into vacuum sufficiently far away from the metal surface [18, 22, 30, 31]. Sufficiently far in this context is defined as large with regards to lattice size and small compared to grain size of the crystal.

Figure 2.6 illustrates the work function for a simple jellium system, where the positive nuclei of the crystal are approximated as semi-infinite uniform charge in the range of $(-\infty, 0)$. Electrons in the solid are confined to a potential well of depth $\Delta V_{\mathrm{inf}} + \Delta V_{\mathrm{surf}}$,

where ΔV_{inf} is the potential in a infinite crystal, arising from electron-ion and electron-electron interactions. The contribution ΔV_{surf} is caused by electrons leaking into the vacuum and producing a dipole density, or the so-called double-layer on the surface. The work function is defined as

$$\phi = \Delta V_{\text{inf}} + \Delta V_{\text{surf}} - E_F, \tag{2.38}$$

where E_F is the Fermi level of the metal.

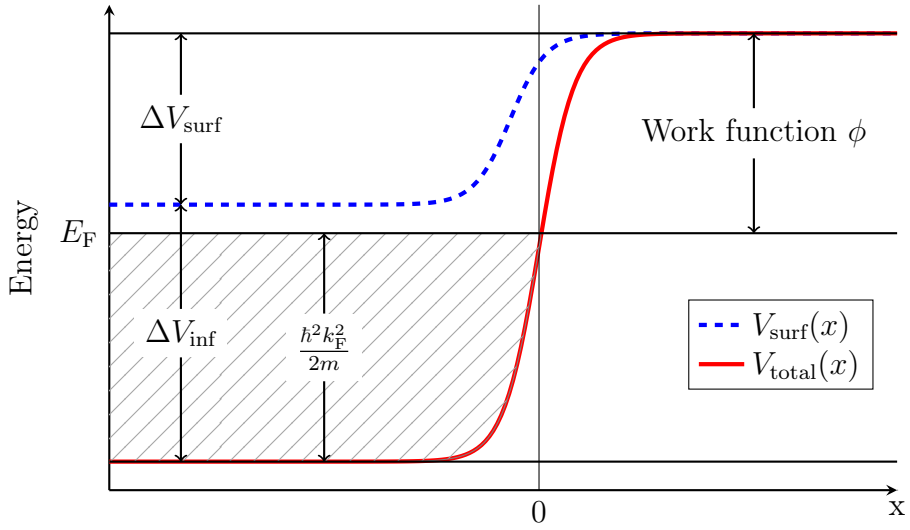

Figure 2.6: Work function definition for a simple jellium system. $V_{\text{total}}(x)$ includes both, the infinite crystal potential and also the surface contribution $V_{\text{surf}}(x)$ due to the double-layer.

The term ΔV_{surf} depends on the properties of the surface and is different for different crystal orientations. In most cases, this can be explained by Smoluchowski smoothing [32], which states that smaller atomic packing density of the crystal surface causes smaller work functions. For a sparse surface, the electronic density tends to fill the space between surface atoms, producing a negative charge density directly under the surface. The surface atoms, which are now missing some electrons, produce a small positive charge density directly over the surface. This dipole layer reduces work function. See Table 2.1 for copper work function dependence on surface orientation. This also explains why the vacuum level distance in the definition of the work function must be small with respect to grain size, otherwise we would obtain an averaged work function over multiple crystal surfaces.

face orientation	ϕ(eV)
(100)	4.59, 4.63
(110)	4.48, 4.50
(111)	4.85, 4.88
(112)	4.53

Table 2.1: Work function data for copper from multiple experiments [33].

The average work function for polycrystalline surface, or a surface consisting of patches with work function ϕ_i and area S_i, can be estimated as [22]

$$\phi_{\text{avg}} = \frac{\sum_i \phi_i S_i}{\sum_i S_i}. \tag{2.39}$$

Here, the work functions of the patches can be thought of as local work functions and in principle, the patches can be scaled even down to atomic level. What determines electron emission (see Section 2.1) in the presence of high applied electric field, is rather the local work function, not the averaged one given by (2.39).

In the widely used Miller and Good WKB theory, described in Section 2.1.3, the transmission probability dependence on energy $D(E, F, \phi)$ is determined by the electric field F and the work function ϕ. In later stages of this work, the effective work function will be deduced from the $D(E, F, \phi)$ versus E curves for a given F, see Section 3.5. The work function ϕ obtained in this way will be called as the work function relevant in transmission or the effective transmission work function.

2.3 Fowler-Nordheim plot analysis

By assuming that the Fowler-Nordheim equation (2.33) holds, the field enhancement β on the surface of the cathode can be estimated from the slope of $\ln(I/E^2)$ plotted against $1/E$, where I is the total measured current and E is the applied field [19, 20, 29]. This method is frequently used by experimentalists.

In this context, the barrier correction factors in the Fowler-Nordheim equation (2.33) are usually approximated as [20]

$$\nu(F) \approx \nu_0 - y_0(F)^2, \tag{2.40}$$

$$\tau(F) \approx \tau_0, \tag{2.41}$$

where ν_0 and τ_0 are constants. By expressing the local electric field in (2.33) as $F = \beta E$, where E is the applied field and by integrating both sides over the emission area, we get

$$\frac{I}{E^2} = \frac{a}{\phi \tau_0^2} \int \beta^2 \exp\left(-\frac{b\phi^{3/2}\nu(\beta E)}{\beta E}\right) dS. \tag{2.42}$$

By introducing β_c (the average, or effective field enhancement) such that

$$\int \beta^2 \exp\left(-\frac{b\phi^{3/2}\nu(\beta E)}{\beta E}\right) dS = \beta_c^2 \exp\left(-\frac{b\phi^{3/2}\nu(\beta_c E)}{\beta_c E}\right) S, \tag{2.43}$$

and taking the logarithm of (2.42), we get

$$\ln\left(\frac{I}{E^2}\right) = -\frac{\nu_0 b\phi^{3/2}}{\beta_c}\frac{1}{E} + \frac{e^3 b}{4\pi\varepsilon_0 \beta_c \sqrt{\phi}} + \ln\left(\frac{a}{\phi\tau_0^2}\beta_c^2 S\right). \tag{2.44}$$

It can be seen from (2.44), that the slope γ of $\ln(I/E^2)$ versus $1/E$, can be used to find the average field enhancement:

$$\beta_c = -\frac{\nu_0 b\phi^{3/2}}{\gamma} \approx -\frac{\left(6.53 \times 10^3 \frac{\text{MV}}{\text{m eV}^{3/2}}\right)\phi^{3/2}}{\gamma}. \tag{2.45}$$

Multiple values for ν_0 have been used in literature, such as 1[2] [34], 0.937 [20], 0.943 [35]. In (2.45) we used $\nu_0 = 0.956$, which was also used in the studies regarding CLIC vacuum breakdowns [12]. The obtained β_c is considered to be good estimation of the maximum β on the cathode surface, due to the exponential weighting in (2.43).

[2] Assumes triangular barrier instead of Schottky-Nordheim.

2.4 Simulation methods

2.4.1 Finite element method

The finite element method (FEM) [36–38] is numerical technique used to solve boundary value problems for partial differential equations. The geometric domain of the problem is divided into non-overlapping simple shaped subdomains or elements, which constitute the mesh and are composed of a number of nodes. In these nodes x_i, so-called shape functions $\phi_i(x)$ are defined such that they satisfy the condition of

$$\phi_i(x_j) = \begin{cases} 1 & \text{if } j = i, \\ 0 & \text{otherwise.} \end{cases} \tag{2.46}$$

In the Galerkin approach, the initial differential equation is weighed by these shape functions and integrated over the whole domain. This results in the weak formulation, which consists of N algebraic equations, where N is the number of nodes in the system. The solution function $u(x)$ is expressed as a linear combination of these same shape functions

$$u(x) \approx u_h(x) = \sum_{j=1}^{N} U_j \phi_j(x), \tag{2.47}$$

where U_j become the unknowns for the problem. Now, with N algebraic equations and N unknowns, the problem can be solved with numerical linear algebra methods. For non-linear partial differential equations, the same approach can be applied, but the resulting system of equations is also non-linear. In this case, a non-linear algorithm, such as the Newton's method must be used to solve the system.

2.4.2 Density functional theory

Density functional theory (DFT) [39] is a computational quantum mechanical method to model the electronic structure of atoms, molecules and condensed phases. The method is used to find the ground state of the many-body time-independent Schrödinger equation within the Born-Oppenheimer approximation [40]

$$\hat{H}\Psi = \left[\sum_{i}^{N} \left(-\frac{\hbar^2}{2m} \nabla_i^2 \right) + \sum_{i}^{N} V_{\text{ext}}(\boldsymbol{r}_i) + \sum_{i<j}^{N} U(\boldsymbol{r}_i, \boldsymbol{r}_j) \right] \Psi = E\Psi, \tag{2.48}$$

where V_{ext} is the external potential due to the stationary nuclei, $U(\boldsymbol{r}_i, \boldsymbol{r}_j)$ is the electron-electron interaction energy and $\Psi = \Psi(\boldsymbol{r}_1, \ldots, \boldsymbol{r}_N)$ is the many-body wave function. Density functional theory is based on the Hohenberg-Kohn theorems [41], which prove that an external potential $V_{\text{ext}}(\boldsymbol{r})$ uniquely determines the density of interacting electrons $\rho(\boldsymbol{r})$. Thus, $\rho(\boldsymbol{r})$ also determines the wave function and all properties of the system. The second Hohenberg-Kohn states that for any particular $V_{\text{ext}}(\boldsymbol{r})$, the exact ground-state energy of the system is the global minimum of an universal energy functional $E[\rho(\boldsymbol{r})]$ and the density that minimises this functional is the exact ground state density $\rho_0(\boldsymbol{r})$. The main problem with these theorems is that the exact form of $E[\rho(\boldsymbol{r})]$ is not known. The energy functional can be represented as

$$E[\rho(\boldsymbol{r})] = T[\rho(\boldsymbol{r})] + \int d\boldsymbol{r} V_{\text{ext}} \rho(\boldsymbol{r}) + \frac{1}{2} \int d\boldsymbol{r} \int d\boldsymbol{r}' \frac{\rho(\boldsymbol{r})\rho(\boldsymbol{r}')}{|\boldsymbol{r} - \boldsymbol{r}'|} + E_{\text{xc}}[\rho(\boldsymbol{r})], \tag{2.49}$$

where all the known terms are written explicitly and the unknown terms are contained within the exchange-correlation functional $E_{\mathrm{xc}}[\rho(\boldsymbol{r})]$.

If an approximate form to $E_{\mathrm{xc}}[\rho(\boldsymbol{r})]$ was known, then the ground state density $\rho_0(\boldsymbol{r})$ can be found by an iteration procedure proposed by Kohn and Sham [42]. First, an initial guess to the density $\rho_0(\boldsymbol{r})$ is made. Then the Kohn-Sham procedure can be expressed through the following equations

$$V_{\mathrm{KS}}(\rho(\boldsymbol{r})) = V_{\mathrm{ext}}(\boldsymbol{r}) + \int d\boldsymbol{r}' \frac{\rho(\boldsymbol{r}')}{|\boldsymbol{r} - \boldsymbol{r}'|} + V_{\mathrm{xc}}[\rho(\boldsymbol{r})], \tag{2.50}$$

$$\left(-\frac{\hbar^2}{2m}\nabla^2 + V_{\mathrm{KS}}(\boldsymbol{r})\right)\varphi_i(\boldsymbol{r}) = \epsilon_i \varphi_i(\boldsymbol{r}), \tag{2.51}$$

$$\rho(\boldsymbol{r}) = \sum_i \varphi_i^*(\boldsymbol{r})\varphi_i(\boldsymbol{r}). \tag{2.52}$$

In (2.50) the Kohn-Sham potential $V_{\mathrm{KS}}(\rho(\boldsymbol{r}))$ is found based on the density guess. Here $V_{\mathrm{xc}}[\rho] \equiv \delta E_{\mathrm{xc}}[\rho]/\delta\rho(\boldsymbol{r})$ is the exchange correlation potential. In (2.51), one particle Schrödinger equations are solved to obtain the non-interacting single particle wave functions $\varphi_i(\boldsymbol{r})$ and finally in (2.52), the new charge density is obtained. This procedure is repeated until the density $\rho(\boldsymbol{r})$ converges and the result is the correct ground state density which solves the many-body Schrödinger equation.

The simplest choice for the exchange-correlation functional $E_{\mathrm{xc}}[\rho(\boldsymbol{r})]$ is the local density approximation (LDA) and it depends only on the electronic density at each point in space. Another group of exchange-correlation functionals is the generalized gradient approximation (GGA), which depends additionally also on the gradient of the electronic density.

2.4.3 Tight-binding quantum transport calculations

Quantum mechanical scattering problems can be solved by describing the system through single-particle tight-binding Hamiltonian [43, 44]. The system consists of a finite scattering region, which has multiple infinite leads connected to it. A tight-binding system is divided into discrete degrees of freedom $|i\rangle$ and the Hamiltonian is expressed as

$$\hat{H} = \sum_{i,j} H_{ij} \left|i\right\rangle \left\langle j\right|, \tag{2.53}$$

where H_{ij} are the elements of the Hamiltonian matrix. The degrees of freedom are usually expressed as $|i\rangle = |\boldsymbol{r}\alpha\rangle$, where $\boldsymbol{r}$ is the coordinate vector of a lattice site and α labels the site's internal degrees of freedom. Hamiltonians of this form can arise directly from an approximate atomic description of a physical system, in which case sites correspond to atoms or molecules. Alternatively, a finite-difference discretization of a continuum Hamiltonian also results in a tight-binding Hamiltonian.

In this section, the wave function formulation of scattering theory is described, which is equivalent to the non-equilibrium Green's function formalism [43]. Due to the translational invariance of the infinite leads, the wave function in them can be expressed as a superposition of the so-called transverse modes

$$\Psi_n(x, y, z) = \frac{1}{\sqrt{L}} \exp(ikx)\chi_n(y, z), \tag{2.54}$$

where we have assumed that the lead is in x direction and in y and z directions it is confined by some potential which determines $\chi_n(y, z)$, where n labels the transversal quantization. In transport calculations with tight-binding systems, these modes in the leads are matched with the wave function in the scattering region and the transmission coefficient is obtained. This is equivalent to solving the Schrödinger equation corresponding to the tight-binding Hamiltonian.

3 Methodology

3.1 Mathematical model for electrical and thermal behaviour of surface defects

3.1.1 System overview

The mathematical model for electrical and thermal behaviour of surface defects imitates the conditions in CLIC accelerating cavities and DC breakdown studies [4, 11, 12]. The system consists of a copper cathode that can have various different surface defects on it, such as protrusions or cavities. In the current work, only single protrusions are studied. The cathode is in vacuum and has an electric field applied to it. The model will describe the resulting local electric field distribution around the cathode, the electric currents inside the cathode defects arising due to emission currents and also the resulting temperature distribution. Time dependence is ignored as the involved electrical and thermal processes reach equilibrium in time much shorter than the accessible experimental time scale [45]. Figure 3.1 shows the schematic for the geometry of the system and the boundary conditions for the differential equations described in the subsequent sections.

The current work improves this mathematical model by including the Nottingham heating (Section 2.1.6) and more accurate emission current evaluation via direct integration of (2.22).

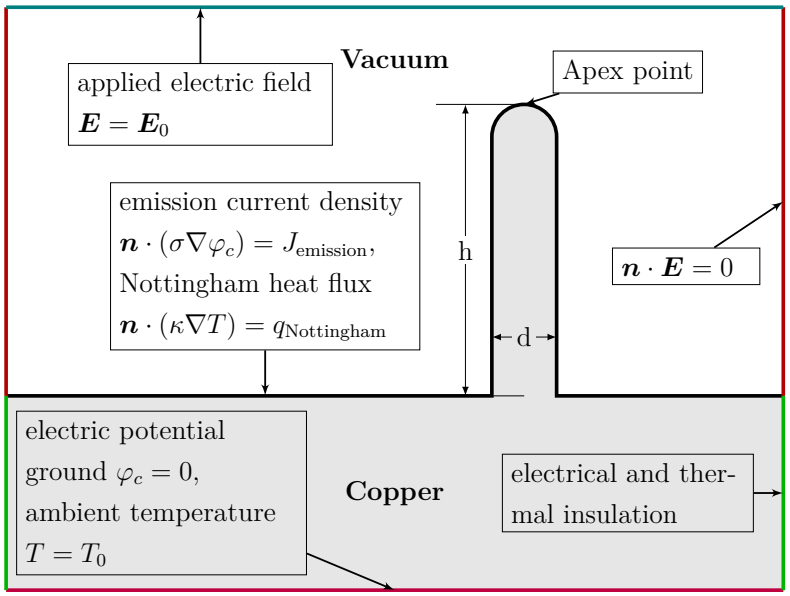

Figure 3.1: Schematic of the modelled system and boundary conditions to the differential equations.

3.1.2 Electric field

In the modelled system (see Figure 3.1), the electric field configuration corresponding to the boundary conditions needs to be found in the vacuum. The configuration also determines the field enhancement β.

The electric potential and field configuration in a system can be found by solving the Laplace equation

$$\nabla^2 \varphi_v(\boldsymbol{r}) = 0, \tag{3.1}$$

where $\varphi_v(\boldsymbol{r})$ is the electrostatic potential in vacuum.

The Laplace's equation (3.1) has three boundary conditions in the system. The top side of the simulation box has the applied external electric field $\boldsymbol{E}_0$

$$-\nabla \varphi_v(\boldsymbol{r}) \equiv \boldsymbol{E}(\boldsymbol{r}) = \boldsymbol{E}_0. \tag{3.2}$$

The sides of the vacuum simulation box have a mirror boundary condition

$$\boldsymbol{n} \cdot (-\nabla \varphi_v(\boldsymbol{r})) \equiv \boldsymbol{n} \cdot \boldsymbol{E}(\boldsymbol{r}) = 0, \tag{3.3}$$

where $\boldsymbol{n}$ is the surface normal vector. The boundary needs to be far enough for it to not affect the field distribution around the defect. The copper-vacuum boundary has a Dirichlet boundary condition

$$\varphi_v(\boldsymbol{r}) = 0, \tag{3.4}$$

due to copper, as a conductive metal, having a constant potential over its surface. The currents inside the metal that cause a small potential difference on the surface, are considered to be negligible when compared to the high potential gradients in vacuum [46].

3.1.3 Electric currents

Electric currents are modelled in the copper domain of the system (see Figure 3.1). The stationary differential equation for finding the potential corresponding to currents can be derived by combining the continuity equation with the differential Ohm's law and is expressed as

$$\nabla \cdot (\sigma \nabla \varphi_c) = 0, \tag{3.5}$$

where $\sigma = \sigma(\boldsymbol{r}, T)$ is the conductivity[1] and φ_c is the electric potential in copper. Equation (3.5) assumes classical diffusive electron transport [44], which holds in systems considerably larger than the mean free path of electrons. In Section 3.1.5, the classical size effect to the conductivities is introduced, which remedies this.

The equation (3.5) has three different boundary conditions in the system. The boundary condition on the copper-vacuum surface corresponds to the electron emission current

$$\boldsymbol{J} \equiv \sigma \nabla \varphi_c = \boldsymbol{J}_0(\boldsymbol{E}, T), \tag{3.6}$$

where $\boldsymbol{J}_0(\boldsymbol{E}, T)$ is the emission current, which is given by (2.22). The bulk sides have a boundary condition corresponding to electrical insulation

$$\boldsymbol{n} \cdot \boldsymbol{J} \equiv \boldsymbol{n} \cdot (\sigma \nabla \varphi_c) = 0, \tag{3.7}$$

and the bottom of the bulk has a boundary condition corresponding to a constant electric potential

$$\varphi_c = 0. \tag{3.8}$$

[1] Spatial dependence comes from the size effects, see Section 3.1.5.

The electrical conductivity of copper $\sigma(T)$ and its temperature dependence are found from data based on the work of Matula [47] and Schuster et al. [48], which has good agreement with experiment from 20 K to the melting point 1356.7 K.

3.1.4 Heating

The temperature distribution is found using the stationary heat equation

$$-\nabla \cdot \big(\kappa \nabla T\big) = J^2/\sigma, \tag{3.9}$$

where $\kappa = \kappa(\boldsymbol{r}, T)$ is the thermal conductivity and J is the current density norm. The right side of (3.9) represents the volumetric resistive heating. The heat equation has three different boundary conditions (see Figure 3.1). The copper-vacuum boundary has the Nottingham heat flux (2.36) boundary condition

$$\boldsymbol{n} \cdot (\kappa \nabla T) = q_{\text{Nottingham}}, \tag{3.10}$$

and the copper bulk side boundary has the boundary condition corresponding to thermal insulation

$$\boldsymbol{n} \cdot (\kappa \nabla T) = 0. \tag{3.11}$$

The bulk bottom boundary has the Dirichlet condition

$$T = T_{\text{amb}}, \tag{3.12}$$

where T_{amb} is the temperature of outer environment; in most cases, $T_{\text{amb}} = 300\,\text{K}$.

The thermal conductivity $\kappa(T)$ and its dependence on temperature is found with the Wiedemann-Franz law [49]

$$\kappa(T) = LT\sigma(T), \tag{3.13}$$

where $L = 2.443 \times 10^{-8} W\Omega K^{-2}$ is the Lorenz number. The law has been found to be valid for copper films above the temperature of 200 K [50].

3.1.5 Classical size effect for conductivities

In a large enough bulk material, the mean free path of electrons is mainly determined by electron-phonon and electron-defect scattering, as electron-electron and electron-boundary scattering are negligible. When the characteristic length, such as the diameter of the protrusion on copper surface or the size of grains (for a polycrystalline solid), is comparable with the bulk mean free path of electrons, boundary scattering becomes important. Subsequently, the electrical conductivity σ and the thermal conductivity κ become size dependent. [51]

The size dependence is usually characterized by the Knudsen number $K_n = \lambda_b/d$, where λ_b is the bulk mean free path of electrons and d is the characteristic length (e.g. the diameter of a protrusion). The size dependent electrical and thermal conductivities can be expressed as

$$\begin{aligned} \sigma_{nano} &= F(K_n) \cdot \sigma_b, \\ \kappa_{nano} &= F(K_n) \cdot \kappa_b, \end{aligned} \tag{3.14}$$

where σ_b and κ_b are the bulk conductivities. The finite size effects correction factor $F(K_n)$ for a thin cylindrical wire can be found using [51]

$$\begin{aligned} F(K_n) &= 1 - \frac{12(1-p)^2}{\pi} \sum_{m=1}^{\infty} m p^{m-1} G(K_n, m), \\ G(K_n, m) &= \int_0^1 \sqrt{1-\xi^2} \int_1^{\infty} \exp\left(-\frac{m\xi t}{K_n}\right) \frac{\sqrt{t^2-1}}{t^4} dt d\xi, \end{aligned} \tag{3.15}$$

where p is the specularity, which is defined as the probability that a boundary scattering event is elastic and specular and it depends on the surface roughness. The specularity value p for copper has been taken to be 0.01 in this work, which is close to the values reported in literature [52–54].

3.2 Finite element method simulations

3.2.1 General info and simulation details

In order to numerically simulate systems based on the mathematical model described in Section 3.1, the finite element method (FEM) (Section 2.4.1) is used. In order to complete the objectives established in Section 1.2 regarding the influence of Nottingham effect and the collective behaviour of multiple emitters, the finite element software COMSOL [55] is employed.

Each FEM simulation consisted of a specific cathode protrusion under a parametrically increasing applied electric field. The simulation is run for increasing applied field values until the maximum temperature in the system reaches $T_{\text{stop}} = 1400\,\text{K}$, which is close to the melting temperature of copper $T_{\text{melt}} = 1358\,\text{K}$. After this temperature, our electrical and thermal conductivity models do not work any more and the protrusion is likely pulled apart by the electrostatic pressure. The other stopping condition is for when the maximum local electric field in the system reaches $F = 14\,\text{GV/m}$, as then, the Schottky-Nordheim barrier (Sec. 2.1.2) is reduced to the Fermi level of the metal and the WKB approximation (Sec. 2.1.3) is not valid. During this calculation, the total emitted current, temperature evolution and total Nottingham and resistive heating powers are outputted.

The FEM simulations are run for a number of different protrusions, each characterized by four parameters: the work function ϕ, tip radius r, height-radius ratio (also known as the aspect ratio) h/r and bottom radius – tip radius ratio r_b/r. Figure 3.2 shows a schematic explaining these parameters and shows three example geometries. The simulations were run for all combinations of the following parameter values:

$$\begin{aligned} \phi &= (3.0,\ 3.5,\ 4.0,\ 4.5)\ \text{eV}, \\ r &= (4,\ 16,\ 64)\ \text{nm}, \\ h/r &= (4,\ 12,\ 20), \\ r_b/r &= (0.25,\ 1.0,\ 4.0), \end{aligned} \tag{3.16}$$

with the Nottingham boundary condition (3.10) included and excluded, for a total of 216 simulations. The parameters were chosen to cover a wide range of different possible defects. The variation of ϕ below the values obtained experimentally for copper (Table 2.1) is verified in the atomic scale work function calculation results. And the work function can also be considerably reduced from $\sim 4.5\,\text{eV}$ due to surface adsorbates [15, 16].

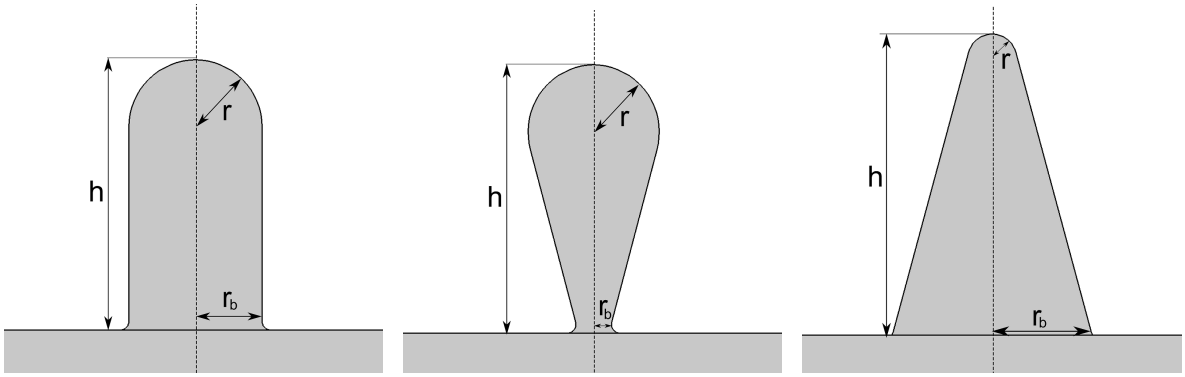

(a) $h/r = 4.0,\ r_b/r = 1.0$ (b) $h/r = 4.0,\ r_b/r = 0.25$ (c) $h/r = 12.0,\ r_b/r = 4.0$

Figure 3.2: Three example system geometries that are solved with FEM. The height of emitter h, tip radius (radius of curvature at the apex) r and the bottom radius or the radius at the foot of the protrusion r_b are shown. The schematics show 2D cross-sections of axis-symmetric 3D protrusions.

The emission current boundary condition (3.6) is evaluated via (2.22) and the Nottingham heat flux boundary condition (3.10) via (2.36). Technical details about these evaluations are described in Section 3.2.2. The ambient temperature boundary condition was $T_{\text{amb}} = 300\,\text{K}$ and all other boundary conditions are fixed according to the mathematical model (see e.g. Figure 3.1).

All of the simulated systems were axis-symmetric and thus a two-dimensional calculation was sufficient for the three-dimensional behaviour.

The boundary distance for all outer boundaries was taken to be far enough for it to not influence the solution near the protrusion. This is easy to accomplish, as the mesh can be very coarse far away from the emitter. All of the outer boundaries were at least $10h$ away from the emitter, where h is the height of the emitter.

3.2.2 Direct numerical emission current and Nottingham effect evaluation

Numerically evaluating the integrals for emission current (2.22) and the Nottingham heat flux (2.36) during a FEM calculation reduces computational performance significantly. Therefore both of the integrals were pre-calculated and tabulated in an uniform grid for a wide range of the three argument values of electric field F, temperature T and work function ϕ. The logarithm of the current density was tabulated, as it varies many orders of magnitude. In FEM simulations, trilinear interpolation is used to evaluate $J(F, T, \phi)$ and $q_{\text{N}}(F, T, \phi)$ with high performance. As both the emission currents and Nottingham heat depend exponentially on the electric field, the logarithms of F were saved uniformly to the tabulated data for optimal accuracy. The range of values for $\ln(F)$ was from $\ln(1 \times 10^{-4})$ to $\ln(14\,\text{GV/m})$ with 200 data points. The range for T was from 200 to 2000 K also with 200 data points and the range for ϕ was from 0.9 to 5.1 eV with 22 data points. The number of data points was chosen such that the estimated interpolation error would be he same for all three parameters. The estimated maximum trilinear interpolation error for the emission current grid was less than 1% in the thermionic and field emission regimes and 15% in the transition regime. This is acceptable, as any small relative uncertainty in

the input parameters can cause orders of magnitude uncertainty in the output parameters due to the exponential nature, considerably outweighing the interpolation error.

3.2.3 Mesh details

To perform the finite element calculations, a triangular mesh was used, generated by COMSOL. Quadratic shape functions were used for all three of the partial differential equations.

Mesh convergence was tested for a few selected simulation parameters by a mesh refinement study with successively more dense meshes. The most important part of the mesh is at the apex of the emitter as it has the highest field enhancement, highest emission currents and most heating. The mesh was chosen such that the total current differed less than 1% from a very high density mesh. This offers good performance with acceptable accuracy. This was achieved with a mesh, which had $\sim$50 elements on the semi-circular boundary at the apex of the emitter.

3.2.4 Solver details

The heating in the system depends on electric currents, emission currents depend on temperature, Nottingham effect depends on temperature and conductivities also depend on temperature. This makes the problem highly nonlinear and a corresponding solvers must be used. In these simulations, Comsol's segregated solver [56] was used and the dependent variables corresponding to the three different partial differential equations were separated into three different segregated steps. In each step, one iteration of the damped Newton's method [56] was performed until the solution converged. To solve the linear systems occurring in the Newton's method, the direct solver PARDISO was used. The relative tolerance, i.e. the euclidean norm of the relative error vector, when solution was accepted was 10^{-6}.

Most simulations in this work were conducted using a parametric sweep over a range of electric fields. The solution to the previous step was used as the initial condition to the next. The parametric stepping method was based on backward differentiation formula with pseudo time as parameter for selecting the electric fields.

3.3 Custom finite element code implementation

A fairly significant amount of effort during this thesis work was put towards developing a custom high-performance finite element code implementing the mathematical model described in Section 3.1. The need arose from atomistic molecular dynamics and kinetic Monte Carlo simulations of surface defects, where the electric field distribution on the surface needs to be known to set the correct surface stress boundary condition. Additionally, the electronic temperature distribution in the metal defect described by the mathematical model can be coupled to the crystal lattice temperature in atomic simulations. Finally, the electronic current distribution can be used to introduce electromigration stress in the atomic simulations. The interfacing of finite element method (FEM) and the atomistic codes is done via software such as FEMOCS [57], developed by Mihkel Veske at the University of Helsinki. FEMOCS provides the 3D mesh from atomistic calculations and the FEM code solves the electrical fields, currents and heating on that mesh.

The FEM code was written in C++ language and was built on top of the library Deal II [58]. Deal II takes care of the shape function mapping, quadrature evaluations, interfacing between high-performance linear solvers and different ways to output the solution.

The Laplace equation (3.1) can be decoupled from the other partial differential equations and solved separately, as the electric field distribution around the defect does not depend on the electric currents or the temperature inside the metal. Solving the Laplace equation is then turned into a linear system of equations in the finite element method formulation, which can be efficiently solved iteratively or by a direct solver. In the developed code, the conjugate gradient method was used.

The other partial differential equations form a coupled non-linear system of equations. To solve this, the Newton's method was implemented. In order to use the Newton's method, the specific weak formulation must be derived. This derivation is given in Appendix B. In addition to this, a large number of smaller details were implemented, such as the emission current and Nottingham effect interpolation from the tabulated data (Section 3.2.2).

Currently, the only thing from the mathematical model (Section 3.1) that is missing from the custom FEM code is the classical size effect of the conductivities. The model in Section 3.1.5 assumes an infinite nanowire and is difficult to apply for a surface consisting of defects with arbitrary geometry, which can result from atomistic calculations.

The corresponding section in results chapter will show the validation of the code against Comsol implementation and a sample output from a mesh generated with FEMOCS.

3.4 Density functional theory calculations

3.4.1 Simulation details

In order to find the possible work function changes near atomistic scale surface defects, density functional theory (DFT) calculation were performed with the Vienna Ab initio Simulation Package (VASP) [59, 60].

An example system geometry can be seen in Figure 3.3. The bulk copper consisted of 5 layers of 56 atoms. The defect was situated on top of the (111) surface. The dimensions of the simulation box were $17.9 \times 17.7 \times 40.0\,\text{Å}^3$. The vacuum distance from the (111) surface was 30 Å. The system was periodic in all directions. This means that we were not studying a single defect, but a surface with a defect per surface area of $316.8\,\text{Å}^2$. The z coordinate of the bottom two layers of the system was fixed at the bulk lattice values, while all other coordinates were fully relaxed with the conjugate gradient method. After relaxation, the full Kohn-Sham potential (2.50) and the Hartree potential, where the exchange-correlation potential is ignored, were outputted. The calculation was performed without any applied electric field and with electric field values of $E_0 = (1, 2, 4)\text{V/nm}$ in the z direction, pointing towards the defect. The dipole correction was turned on to avoid interactions between periodically repeated images.

All investigated geometries are shown in Figure 3.4. A wide variety of different defects was chosen to see the possible effects on the work function. Some of the geometries, such as a single adatom and the planar defect exist very frequently in real systems, while the sharper defects have higher energy and in real systems should quickly diffuse to shallower geometries. However, these sharper defects can also be present in metastable or intermediate configurations, such as when a surface is the middle of a dynamic process.

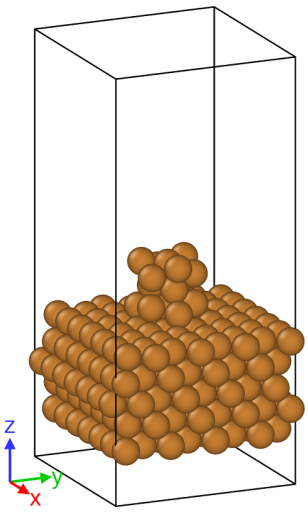

Figure 3.3: Example system of the density functional calculations corresponding to the Extrusion 1 geometry. The bulk consists of 5 layers of atoms and the defect is situated on top of the (111) surface.

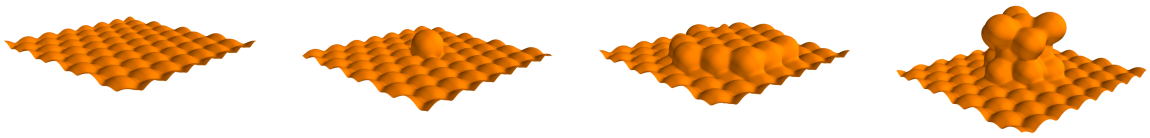

(a) Clean surface (b) Single (c) Planar (d) Extrusion 1

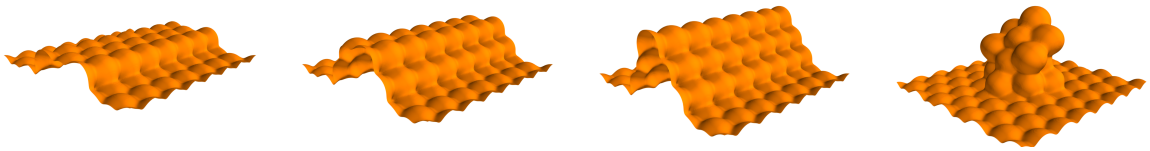

(e) Extrusion 2D 1 (f) Extrusion 2D 2 (g) Extrusion 2D 3 (h) Extrusion 2

Figure 3.4: Studied geometries. An equipotential surface of the electron potential energy near the metal–vacuum boundary is shown for each geometry. The 2D geometries will produce infinitely extending continuous lines due to the periodic boundary conditions.

Nevertheless, it is instructive to see how each of the geometries affects the work function, even if their existence is rare.

3.4.2 Solver details

The calculations were performed with the Vienna Ab initio Simulation Package (VASP) [59, 60]. The Perdew-Burke-Ernzerhof (PBE) [61] generalized gradient exchange-correlation functional was used. To solve the Kohn-Sham equations (2.50)–(2.52), the projector augmented wave method was used. All calculations were carried out with a 500 eV kinetic energy cutoff for the plane wave basis set. Monkhorst-Pack meshes with $(2 \times 2 \times 1)$ $\boldsymbol{k}$-points were used, where the z coordinate of all of the k-points was zero, due to slabs

being decoupled from each other in the periodic z direction.

3.4.3 Conventional work function calculation

Conventionally, the work function of a surface is calculated by averaging the Hartree potential in x and y directions (see Figure 3.3 for the coordinate system) for the system without any electric field applied. This averaged potential in the vacuum, sufficiently far away from the surface for it have plateaued, is then considered as the vacuum level and compared to the Fermi level of the metal to obtain the work function [17]. Hartree potential is used here, because it converges much faster to the vacuum level than the full Kohn-Sham potential. The exchange-correlation potential only introduces the image charge interaction (see Section 2.1.2), which pulls the electron back to the metal, but does not affect the potential energy far from the surface.

In cases with electric field applied, this conventional approach can not be used, as electric field affects the potential energy in the vacuum. Some other method must be used and the exchange-correlation potential must be included in the analysis, as the exact shape of the potential becomes important.

3.5 Work function determination from transmission probability dependence on energy

In the one dimensional case, within the WKB approximation presented in Section 2.1.3, the transmission probability $D(E, F, \phi)$ dependence on electron energy E is solely determined by the electric field value F and the work function of the surface ϕ. It is possible to turn this around and determine the work function ϕ based on the transmission probability dependence on energy $D(E)$ and the electric field.

Let us assume that the transmission probability $D(E, F, \phi)$ dependence on electron energy E was known for two different surfaces, with a known work function ϕ_0 and an unknown work function ϕ_1 for a known electric field F. Let us investigate the equation

$$D(E_F, F, \phi_1) = D(E_0, F, \phi_0), \tag{3.17}$$

which states that the transmission probability of the unknown surface at Fermi energy is equal to the transmission probability for the known surface at an unknown energy value E_0. In (3.17), $E_0 - E_F$ represents energy value by which one curve needs to be shifted, such that both curves match at the Fermi level. By using (2.16), the equation simplifies to

$$\phi_1^{3/2}\nu(y(E_F, \phi_1)) = (\phi_0 + E_F - E_0)^{3/2}\nu(y(E_0, \phi_0)), \tag{3.18}$$

$$E_0 - E_F = \phi_0 - \phi_1 \left(\frac{\nu(y(E_F, \phi_1))}{\nu(y(E_0, \phi_0))} \right)^{2/3}. \tag{3.19}$$

If

$$E_0 - E_F = \phi_0 - \phi_1 \tag{3.20}$$

holds, then $y(E_F, \phi_1) = y(E, \phi_0)$ (see (2.17)) and therefore also (3.19) holds.

Equation (3.20) states that the energy value E_0, where the transmission probability of surface with ϕ_0 is the same as the transmission probability of surface with ϕ_1 at Fermi level, directly determines the difference between the work functions of the surfaces. In

other words, the energy value by which one $D(E)$ curve needs to be shifted such that both curves match at Fermi level is the difference between the work functions of both curves. This result is illustrated in Figure 3.5.

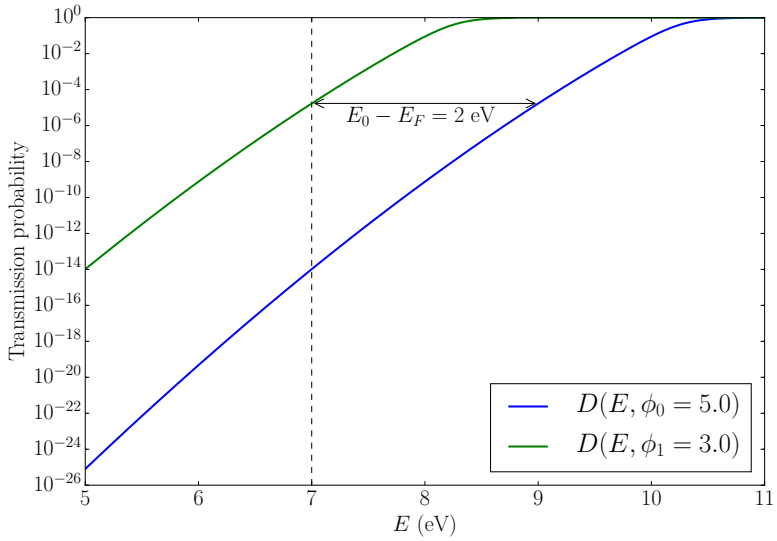

Figure 3.5: Work function determination from transmission probability dependence on energy curves. Both curves were calculated via (2.13). Fermi energy is 7 eV.

3.6 Tight-binding quantum transport calculations

As described in Section 3.5, the work function for potential landscapes obtained from density functional theory with an applied electric field can be determined from the transmission curves through the three dimensional surface potential barrier given by the full Kohn-Sham potential.

To find the transmission probability dependence on electron energy, tight binding quantum transport method is employed, see Section 2.4.3 for the theory. Kwant code [43], developed by researchers in the Delft University, is used.

The potential energy landscape obtained from density functional theory calculations is clamped 3 eV below the Fermi level at a constant level. This extra energy range is included to The linearly decreasing potential in the vacuum is extended to also reached this level. This is because we only need the tunnelling probability at Fermi level and at higher values for the reference curve and the shape of the potential far below these energy values does not influence the transmission. The reference transmission curve is taken to be the clean surface, which is assumed to have a constant work function independent from the electric field. In metal and vacuum, away from the barrier, the free electron model is assumed. This means that the electrons incident on the surface barrier and also the transmitted electrons are plane waves. Taking all of this into account, the Hamiltonian of the transmission problem is

$$\hat{H} = -\frac{\hbar^2}{2m}\nabla^2 + V_{\text{barrier}}(\boldsymbol{r}), \tag{3.21}$$

where $V_{\text{barrier}}(\boldsymbol{r})$ is the surface potential barrier obtained from density functional theory.

To turn the Hamiltonian given in (3.21) into a tight-binding Hamiltonian, the geometric domain is discretized into an uniform grid with spacing a and the finite difference approximation of the gradient operator is used. The resulting tight-binding Hamiltonian is

$$\begin{aligned}\hat{H} = \sum_{i,j,k}[(V_{\text{barrier}}(ai, aj, ak) + 6t)\,|i,j,k\rangle\,\langle i,j,k| - \\ -t(\,|i+1,j,k\rangle\,\langle i,j,k| + |i,j,k\rangle\,\langle i+1,j,k| + \\ + |i,j+1,k\rangle\,\langle i,j,k| + |i,j,k\rangle\,\langle i,j+1,k| + \\ + |i,j,k+1\rangle\,\langle i,j,k| + |i,j,k\rangle\,\langle i,j,k+1|)],\end{aligned} \tag{3.22}$$

where i, j, k label the discrete lattice sites, $|i,j,k\rangle$ is the discrete positional state corresponding to lattice site and $t \equiv \hbar^2/(2ma^2)$. The lattice spacing was chosen to be $a = 0.05\,\text{nm}$ to represent the details of the potential with sufficient accuracy. The maximum energy of a plane wave that can accurately be described by this mesh is $\hbar^2/2ma^2 \approx 42\,\text{eV}$, which is more than enough for our application. The mesh convergence was tested by comparing the results with a $a = 0.03\,\text{nm}$ mesh for a few select cases and was found to be satisfactory.

With the use of Kwant, periodic boundary conditions were applied in the directions parallel to the metal surface. In metal and vacuum, normal to the metal surface, infinite leads were attached. The periodic boundary conditions in the transversal directions introduce an infinite amount of modes in the lead, with different transversal quantization energies. All but the first mode, with zero transversal quantization energy, are ignored. The transmission coefficient of the first mode with the specified energy in the metal input lead to all modes in the vacuum lead was calculated. The transmission coefficient was calculated for energy range of $-3\,\text{eV}$ to $5\,\text{eV}$ with respect to the Fermi level and with a step of $0.1\,\text{eV}$.

4 Results and discussion

4.1 Custom finite element code validation and output

The developed custom finite element C++ code was compared with the equivalent Comsol implementation. Same mesh was used in both cases. The results of this comparison are shown in Figure 4.1. The system for comparison was a two dimensional protrusion with dimensions ($h = 6\,\mathrm{nm}, r = 1\,\mathrm{nm}$) and the applied electric field was $E_0 = 4\,\mathrm{V/nm}$. As the C++ implementation, at this moment did not support finite size effects to electrical and thermal conductivities, they were not included. Other than that, the complete mathematical model described in Section 3.1 was solved. The comparison was done with linear shape functions, which explains the noticeable roughness in electric field and current density solutions. The distributions and maximum values of electric field norm, current density norm and temperature match very well. The estimation of electric field enhancement being equal to the height divided by radius of the protrusion does not hold in two-dimensional cases.

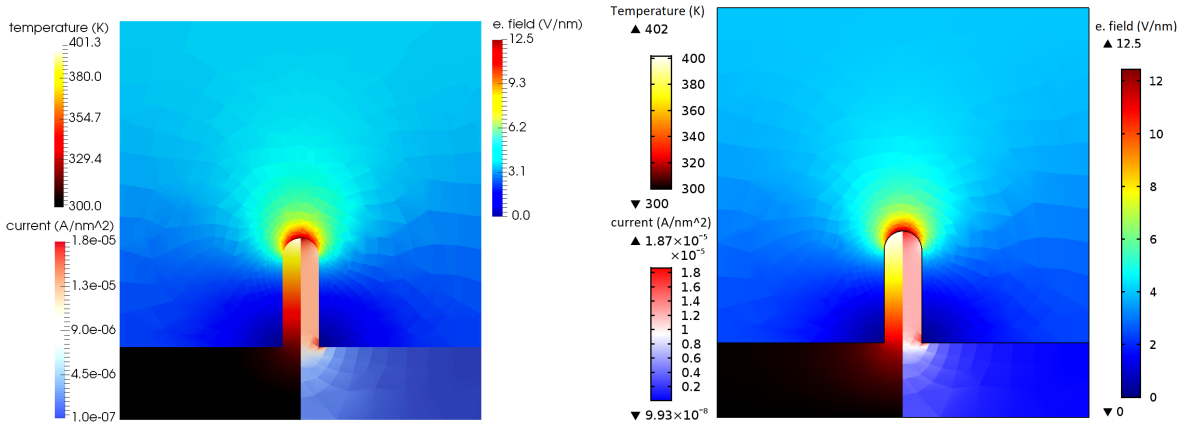

(a) C++ code (b) COMSOL

Figure 4.1: Comparison of the C++ finite element code against a Comsol implementation. The mesh is the same in both cases, protrusion dimensions are ($h = 6\,\mathrm{nm}, r = 1\,\mathrm{nm}$) and the applied electric field is $E_0 = 4\,\mathrm{V/nm}$. The size effects are ignored in both cases. The C++ code results were visualized with Paraview.

This C++ implementation is used by colleagues working on merging molecular dynamics and kinetic Monte Carlo simulations with finite element calculations. Figure 4.2 shows an example calculation, where the mesh was generated from a molecular dynamics simulations by FEMOCS [57], a software being developed by Mihkel Veske. The protrusion dimensions were ($h = 480\,\mathrm{nm}, r = 40\,\mathrm{nm}$), work function was assumed to be $\phi = 4.5\,\mathrm{eV}$ and the applied electric field was $E_0 = 1.5\,\mathrm{V/nm}$. The local field at the apex in this case

was $\sim 13\,\mathrm{V/nm}$, which was reduced from ideal case due to simulation box size and the fairly coarse mesh at the apex. The resulting temperature at the apex was 577 K, which is lower than the full mathematical model would predict, due to the absence of conductivity size effects.

The resulting C++ finite element code is also published in a GitHub repository [62] and will see development and improvements in the future.

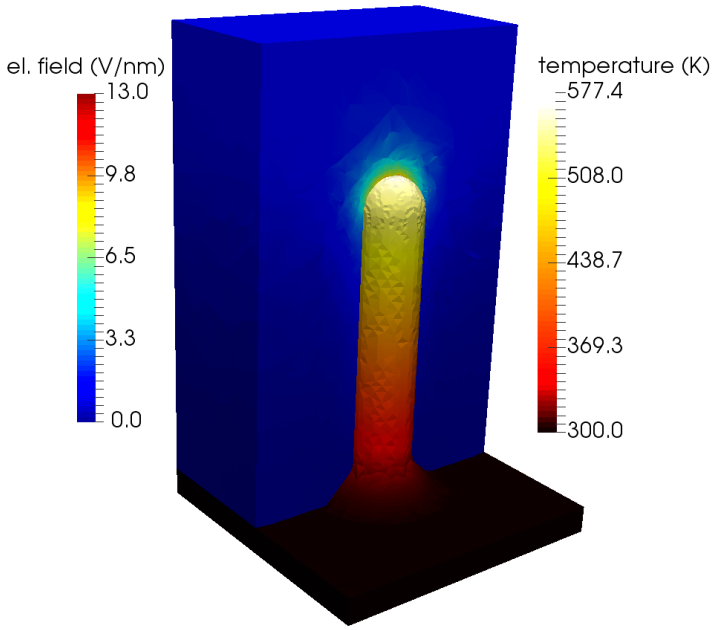

Figure 4.2: C++ code ran for a system generated from FEMOCS [57] (developed by Mihkel Veske, Helsinki University). The protrusion dimensions are ($h = 480\,\mathrm{nm}, r = 40\,\mathrm{nm}$) and the applied electric field is $E_0 = 1.5\,\mathrm{V/nm}$. Visualization produced with Paraview.

4.2 Influence of the Nottingham effect

Figure 4.3 shows the influence of the Nottingham effect for three different emitters with equivalent geometry but varying work function. The radius of the emitters was $r = 16\,\mathrm{nm}$, aspect ratio was $h/r = 12$, top–bottom radius ratio was $r_b/r = 1.0$ and the work function ϕ was varied from 3.5 to 4.5 eV. For all three work function ϕ values, the Nottingham effect contributes more heating than ohmic and the applied melting electric field value, or in other words, the applied electric field value which causes the emitters to melt, is reduced significantly.

Figure 4.4 shows the same dependencies as Figure 4.3, but here the aspect ratio of the emitters is varied instead of the work function. The work function of the emitters was 3.5, radius of the emitters was $r = 64\,\mathrm{nm}$ and top–bottom radius ratio was $r_b/r = 0.25$. In these cases, the Nottingham heating power starts to decline before melting temperature is reached and ohmic heating causes the emitter to melt. In case of the higher aspect ratios, the Nottingham heating even approaches zero and the melting field (applied field, which causes the emitter to melt) is practically unchanged due to the Nottingham effect. This is because the parameters for these emitters were chosen to hamper the heat flow into the bulk material, most of the emitter heats up considerably and starts to emit thermally excited electrons. In principle, if the heat flow from the protrusion into bulk was reduced

even further, for example by reducing r_b/r, then the Nottingham effect should start to cool the emitter and the melting field would be increased with the inclusion of the Nottingham effect. These cases are, however, tricky to simulate, as both the ohmic and Nottingham heating dependence on electric field become very sharp and numerical algorithms tend to have trouble converging. But if Nottingham cooling was occurring in a system, then it would not affect significantly the melting field obtained with only ohmic heating, as ohmic heating scales with the square of the current density (see (3.9)) and Nottingham heat scales linearly with current density (see (2.37)).

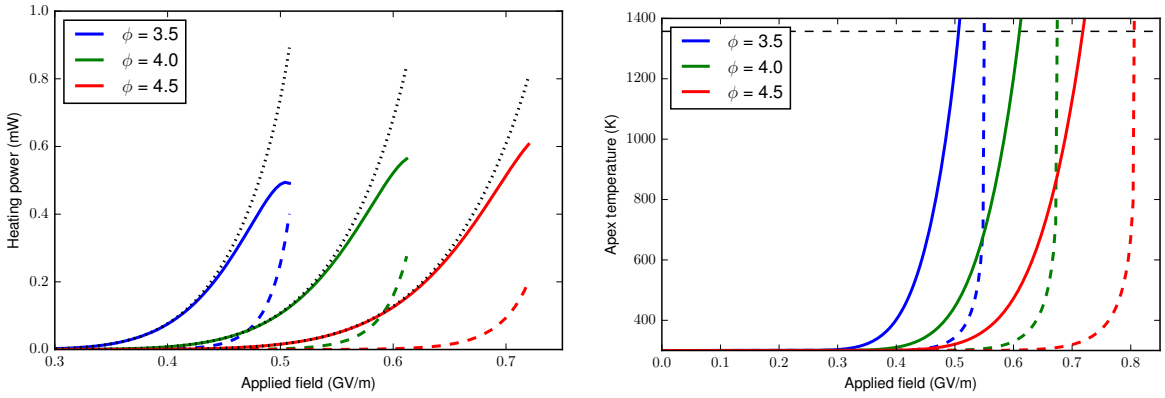

(a) (b)

Figure 4.3: Nottingham effect influence for an emitter with parameters $r = 16\,\text{nm}$, $h/r = 12$, $r_b/r = 1.0$ and varying ϕ. Panel (a) shows the total Nottingham (solid lines) and ohmic heating power dependence on the applied electric field. Dotted black lines show the addition of the two contributions. Lines end, when the system reaches melting temperature. Panel (b) shows the apex temperature dependence on the applied electric field with the Nottingham effect included (solid lines) and excluded (dashed lines). The black dashed line shows the melting temperature of copper. Nottingham effect contributes more to the total heating than ohmic and considerably reduces the applied field value, when the emitter melts.

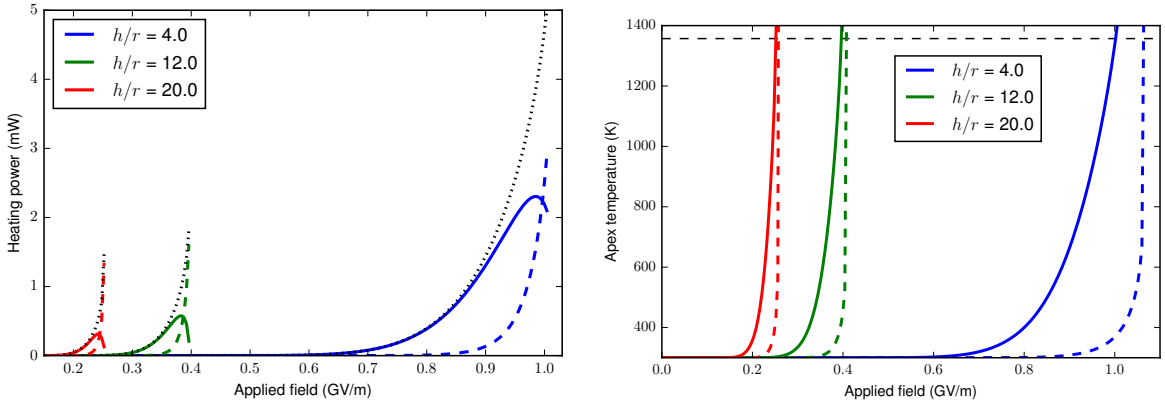

(a) (b)

Figure 4.4: Same as Figure 4.3, but the simulated emitter parameters were $\phi = 3.5\,\text{eV}$, $r = 64\,\text{nm}$, $r_b/r = 0.25$ and varying h/r.

ϕ	r	$\frac{h}{r}$	$\frac{r_b}{r}$	$\frac{P_{\text{Not}}}{P_{\text{ohm}}}$	$E_{\text{melt,N}}$	E_{melt}	ΔE_{melt}	$F_{\text{melt,N}}$	F_{melt}	ΔF_{melt}	%
4.0	16	12	1.00	2.04	0.61	0.67	0.06	8.26	9.11	0.85	9.3
3.5	16	12	1.00	1.22	0.51	0.55	0.04	6.86	7.43	0.57	7.7
4.5	16	12	1.00	3.02	0.72	0.81	0.09	9.72	10.88	1.16	10.7
4.0	4	12	1.00	2.66	0.64	0.72	0.08	8.64	9.69	1.05	10.9
4.0	64	12	1.00	1.31	0.56	0.60	0.04	7.56	8.13	0.57	7.1
4.0	16	4	1.00	4.43	1.54	1.81	0.28	9.68	11.43	1.74	15.3
4.0	16	20	1.00	1.35	0.39	0.42	0.03	7.75	8.37	0.62	7.4
4.0	16	12	0.25	0.75	0.52	0.54	0.03	7.04	7.43	0.39	5.3
4.0	16	12	4.00	5.44	0.80	0.96	0.17	10.14	12.27	2.13	17.3
3.0	64	20	0.25	0.03	0.20	0.20	0.00	4.04	4.08	0.05	1.2
3.0	16	4	4.00	6.79	1.41	1.90	0.49	8.09	10.90	2.81	25.8

Table 4.1: The dependence of the influence of the Nottingham effect on emitter parameters. The first four columns determine the emitter parameters, where the work function ϕ is in eV and radius is in nm. The next columns show data about the influence of the Nottingham effect. $P_{\text{Not}}/P_{\text{ohm}}$ is the ratio of the total Nottingham and ohmic heating power at melting temperature, $E_{\text{melt,N}}$ is the applied melting field (field which causes the emitter to melt) with Nottingham effect included, E_{melt} is the applied melting field without Nottingham effect, ΔE_{melt} is the difference between the last two columns, and the next three columns are the corresponding maximum local electric fields. All electric fields are given in GV/m. The last column shows by how many percent does the addition of the Nottingham effect reduce the melting field. This percent is the same for applied and local field. The first row is a reference emitter and the next four pairs of emitters all correspond to varying one parameters with respect to the reference. The last two rows show the extremal behaviour out of all the simulations.

From Figure 4.3, it can be seen that increasing work function increases the relative influence of the Nottingham effect. Figure 4.4 shows that increasing the aspect ratio of the emitters reduces the influence of the Nottingham effect. Table 4.1 shows how each of the four parameter affects the relative influence of the Nottingham effect. For the reference emitter, with parameters $\phi = 4.0\,\text{eV}$, $r = 16\,\text{nm}$, $h/r = 12$ and $r_b/r = 1$, near melting temperature, Nottingham heating power is double the ohmic heating power and inclusion of the Nottingham effect reduces the melting field by 9.3%. The same data is also shown in Figure 4.3. In each next pair of rows, one of the four parameters is varied. Increasing the radius of the emitter reduces the influence of the Nottingham effect, as expected, because Nottingham heating power scales with the surface area and ohmic heating scales with the volume of the emitter. But even for $r = 64\,\text{nm}$, the melting field reduction of 7% is considerable. However, for emitters with $r > 1\,\mu\text{m}$, Nottingham effect can safely be ignored due to this scaling. Increasing the bottom radius of emitter considerably increases the relative power of the Nottingham effect, as the volumetric ohmic heat easily escapes the emitter and does not affect the temperature at the apex very significantly. The Nottingham heat, however, is produced right at the surface and directly heats the apex point. The protrusions which have a narrow connection with the bulk also model grain boundaries between the defect and the bulk (such as a copper nanoparticle on the surface would have).

The last two rows of Table 4.1 also show the emitters for which Nottingham effect influenced temperature the least and the most out of all the simulated parameter combinations. The emitter with parameter values of $\phi = 3.0\,\text{eV}$, $r = 64\,\text{nm}$, $h/r = 20.0$, $r_b/r = 0.25$ had a very negligible contribution of the Nottingham effect at melting temperature, as expected from previous discussion. The parameter combination of $\phi = 3.0\,\text{eV}$, $r = 16\,\text{nm}$, $h/r = 4$, $r_b/r = 4.00$ was influenced by the Nottingham effect the most. This is because many combinations, such as $\phi = 4.5\,\text{eV}$, $r = 4\,\text{nm}$, $h/r = 4$, $r_b/r = 4.00$ failed to reach melting temperature within the specified local electric field range of up to $14\,\text{GV/m}$.

4.3 Effect of multiple emitters on the Fowler-Nordheim plot

Realistic cathodes have many different surface defects on them and all are emitting current under an applied electric field. In this section, the collective behaviour of all the simulated emitters corresponding to all combinations of the parameters given in (3.16) is investigated. When an emitter reaches the melting temperature of copper, it is assumed to be evaporated and excluded from the subsequent current emission. This produces current spikes when emitters start to melt. It is assumed that there is exactly one of each emitter, which does not correspond to any realistic distribution, but this analysis still provides insight into possible collective effects which can occur with any statistical emitter distribution.

The collective emission current from all of the emitters is shown in Figure 4.5(a) and the corresponding Fowler-Nordheim plot in 4.5(b). The slope of the Fowler-Nordheim plot for lower electric fields is determined by the single best-emitting defect. When this defect melts, then Fowler-Nordheim plot becomes determined by the next-best emitter, which also quickly melts due to being similar to the previous emitter. This behaviour produces a curve, which can have an arbitrary shape, depending on the statistical distribution of different emitters. The deviation from the straight line starts when the first emitter melts, which happened for the applied electric field value of $E = 200\,\text{MV/m}$, also seen in Table 4.1. In real systems, this deviation can start at much lower fields, as sharper defects may be present or defects might be located on top of each other. Additionally, in nanoscale systems, the melting temperature can be considerably reduced [63, 64]. If a melting temperature of $T_{\text{melt}} = 600\,\text{K}$ was assumed instead of the bulk copper melting temperature, then the deviated curve would start at the applied field value of $E = 180\,\text{MV/m}$.

The red curve in 4.5(b) is a smoothed version of the collective Fowler-Nordheim plot, that can occur in realistic systems due to a wider availability of different emitters and possible dynamic changes of the emitters during melting. In the pre-melting region, the slope of the Fowler-Nordheim plot is determined by the emitter with parameter values of $\phi = 3.0\,\text{eV}$, $r = 64\,\text{nm}$, $h/r = 20.0$, $r_b/r = 0.25$ and with a real field enhancement value of $\beta = 20$. If the Fowler-Norhdeim plot analysis, given by (2.45), was used with the assumption of $\phi = 4.5\,\text{eV}$, as is done in experimental studies, then the obtained estimated field enhancement would be $\beta_c = 36$. In the deviated part of the curve, this analysis can give arbitrarily large values of β_c. For example, near $E = 250\,\text{MV/m}$, the estimated field enhancement is $\beta_c = 100$. This behaviour can also possibly explain the curvature in the experimental Fowler-Nordheim plots shown in Figure 1.3.

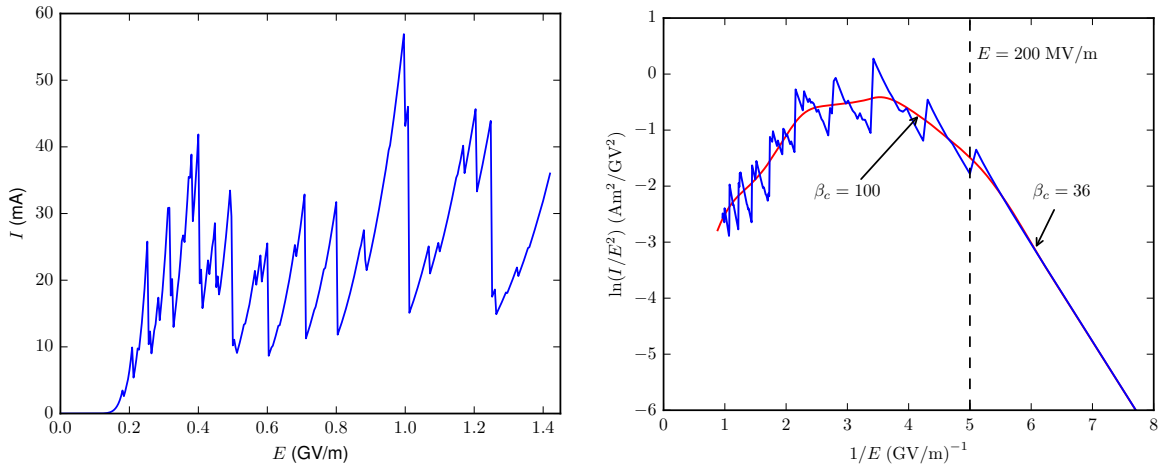

(a) Total current

(b) Fowler-Nordheim plot

Figure 4.5: The collective emission current from all simulated emitters (a) and the corresponding Fowler-Nordheim plot (b). In (b), the red line is obtained by Savitzky-Golay smoothing of the original blue line. The labels corresponding to the estimated field enhancements β_c were obtained from the slope of the smoothed curve via (2.45) with the assumption of $\phi = 4.5\,\mathrm{eV}$.

4.4 Potential landscapes from density functional theory

Figure 4.6 shows an example potential landscape output from the density functional theory calculations for the geometry of Extrusion 2. The potential slice plotted was taken from the middle of the defect, as shown in Figure 4.6(b). In Figure 4.6(a), the potential slice is elevated according to the value of the potential. In vacuum, away from the defect, the small kink in potential represents the dipole correction imposed by VASP to suppress the interaction between the periodically repeating images. The potential shape below the Fermi level and the dipole correction are not important for work function determination and therefore will be left out from the subsequent discussion.

In Figure 4.7, the potential slices are clamped by Fermi level and only the interesting area of metal-vacuum transition is left in the figure. Potential distributions for all electric field values for the clean surface and extrusion 2 geometry are shown. In case of $E = 0\,\mathrm{V/nm}$, both potential distributions converge to a constant value in vacuum and the converged value for extrusion 2 is smaller than the clean surface value. This is explained by Smoluchovki smoothing (Section 2.2), which states that reduced packing density at the surface causes reductions in work function. All of the studied defects cause the packing density to decrease with respect to (111) surface and a work function reduction results.

Figure 4.7 also compares the potential distributions for the extrusion 2 defect and clean surface with applied electric field. In case of clean surface, with the application of electric field, the potential barrier behaves similarly to the Schottky-Nordheim barrier described in Section 2.1.2. The height of the barrier reduces uniformly and smoothly with increasing electric field. In case of the defect, the surface barrier near the tip of the defect is reduced much more than at the foot of the defect with increasing electric field. In case of $E = 4\,\mathrm{V/nm}$, the potential barrier near the apex even starts to approach the Fermi level. But interestingly, at the base of the defect, the potential barrier is higher than

the corresponding clear surface barrier. Additionally, the barrier is slightly wider for the defect. But even when this seemingly big hole exists in the surface barrier, the electrons trying to escape the metal are described by plane waves, which need to tunnel through the barrier as a whole.

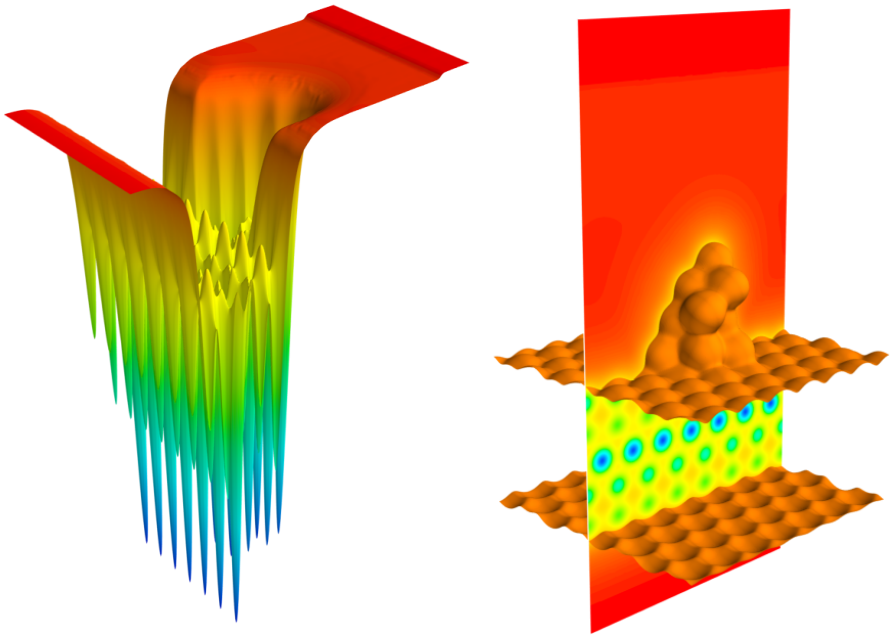

(a) (b)

Figure 4.6: Potential slice from density functional theory calculations. In (a), the potential energy dependence is extruded. The small kink in vacuum represents the DFT dipole correction. Panel (b) shows the position of the slice with respect to the metal boundaries. In both cases, the full Kohn-Sham potential is shown.

4.5 Conventional work function calculation

The conventional work function calculation with density functional theory assumes no external electric field is applied and the 3D potential around the defect is averaged in planes parallel to the surface, as described in Section 3.4.3. The averaged potential for all of the defects is shown in Figure 4.8. In this figure, the exchange-correlation potential was excluded, as it converges slower to the vacuum level due to the image charge effect. Each potential reaches constant value in the vacuum. The difference between this vacuum level and Fermi level is the work function by definition, see Section 2.2. The results for all of the defects are given in Table 4.2. The result for the clean (111) surface, 4.84 eV matches well with values obtained from literature, see Table 2.1. As expected, in the case of defects, the work function is reduced with respect to the clean surface, due to the reduction of surface atomic packing density (Smoluchowski smoothing). Sharper geometries produce a higher work function decrease than shallower ones. The largest work function decrease was for Extrusion 1, where the work function decreased by 12.0%. Of course, it is important to keep in mind that the system was periodic, so the system consisted of a high density of these defects, but the local work function close to one single isolated defect should match with these values.

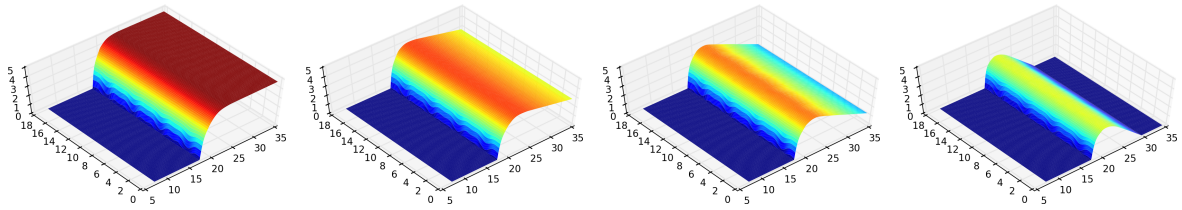

(a) $E = 0\,\mathrm{V/nm}$ (b) $E = 1\,\mathrm{V/nm}$ (c) $E = 2\,\mathrm{V/nm}$ (d) $E = 4\,\mathrm{V/nm}$

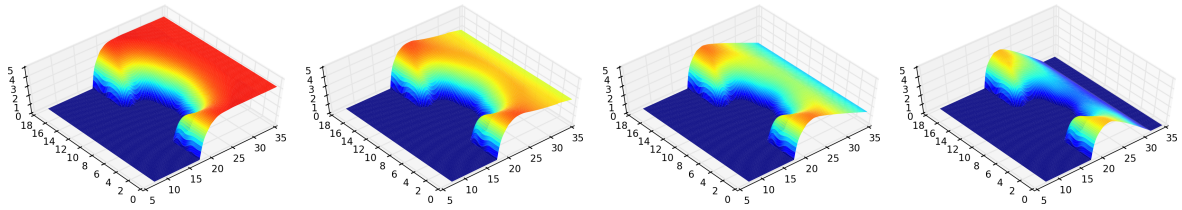

(e) $E = 0\,\mathrm{V/nm}$ (f) $E = 1\,\mathrm{V/nm}$ (g) $E = 2\,\mathrm{V/nm}$ (h) $E = 4\,\mathrm{V/nm}$

Figure 4.7: Potential slices for the calculated electric field values, where the vacuum dipole correction is cut and the potential is clamped to Fermi level. The slices were taken from the middle of the simulation box, as in Figure 4.6. Panels (a)–(d) show potential barriers for clean surface and (e)–(h) for Extrusion 2. The z axis (elevation direction) shows potential energy values in eV and x, y axis show spatial dimensions of the potential slice, in Å.

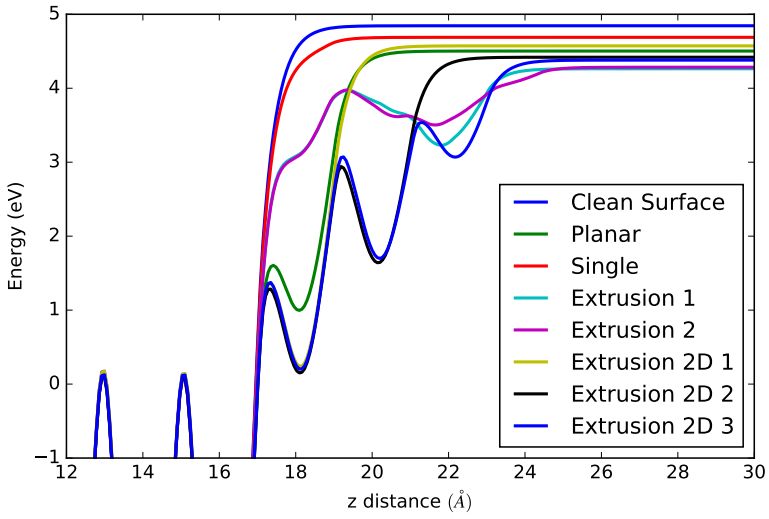

Figure 4.8: Potential averaged over planes parallel to the surface for all defects near the metal-vacuum transition. Unimportant parts, e.g. dipole correction and potential deep in metal are cropped. The potential used here is the Hartree potential, which excludes the exchange-correlation interaction, as converges faster in vacuum and is slightly more accurate. Potential is given with respect to Fermi level.

Geometry	ϕ	$\Delta\phi$
Clean surface	4.84	0.00
Planar	4.50	0.34
Single	4.69	0.15
Extrusion 1	4.26	0.58
Extrusion 2	4.28	0.56
Extrusion 2D 1	4.57	0.27
Extrusion 2D 2	4.42	0.42
Extrusion 2D 3	4.38	0.46

Table 4.2: Work function results from conventional work function calculations. The work function ϕ is given in eV and $\Delta\phi$ shows the reduction with respect to the clean surface.

4.6 Effective work function dependence on electric field

It is clear from Figure 4.7 that for the defective surface, the potential barrier for electron emission depends very differently from electric field then for the clean surface. The surface potential barrier of the clean surface depends on the electric field analogously to the Schottky-Nordheim barrier and the work function value is assumed to be independent of the applied electric field. To investigate the work function for other geometries, the method described in Section 3.5 can be employed, if the transmission probability dependence on electron energy is known.

To obtain the transmission probability curves, tight-binding quantum transport calculations were used on the three dimensional potential barriers obtained from density functional theory, as described in Section 3.6. The results are shown in Figure 4.9. The general shape of the curves matches well with the transmission probability curves obtained from the one dimensional WKB approximation shown in Figure 2.3. There are, however, differences near the top of the surface barrier, but that region is irrelevant to the current analysis. Additionally, the relevant emission mechanism for field emitters is field emission, where most of the emitted electrons originate from the Fermi level.

The curves in Figure 2.3 divide into three groups by slope: the steepest curves correspond to electric field of $E = 1\,\mathrm{V/nm}$, the next ones to $2\,\mathrm{V/nm}$ and the shallowest ones to $4\,\mathrm{V/nm}$. For each electric field value, clean surface has the lowest transmission probability, corresponding to highest work function. By employing the method described in Section 3.5, the effective work function that determines the electron emission probability at Fermi level is obtained for the defective surfaces from the shift in energy with respect to the corresponding clean surface curve. The results are given in Table 4.3 and visualised in Figure 4.10. In some cases, there is an increase in work function when electric field is turned on at $1\,\mathrm{V/nm}$, which can be caused by the slight widening of the surface barrier, as can be observed in Figure 4.7 for the $E = 4\,\mathrm{V/nm}$ case. This effect is not present in the case without electric field. On the other hand, the work function values at $E = 0\,\mathrm{V/nm}$ and $E = 1\,\mathrm{V/nm}$ match fairly well, which validates the developed work function methodology based on the quantum transport calculations. In all cases, increasing the electric field from $1\,\mathrm{V/nm}$ decreases the work function. Highest decrease of work function occurs for the Extrusion 2 geometry, for which at $E = 4\,\mathrm{V/nm}$, the work function was decreased by $1.31\,\mathrm{eV}$ or 27.1% with respect to the clean surface.

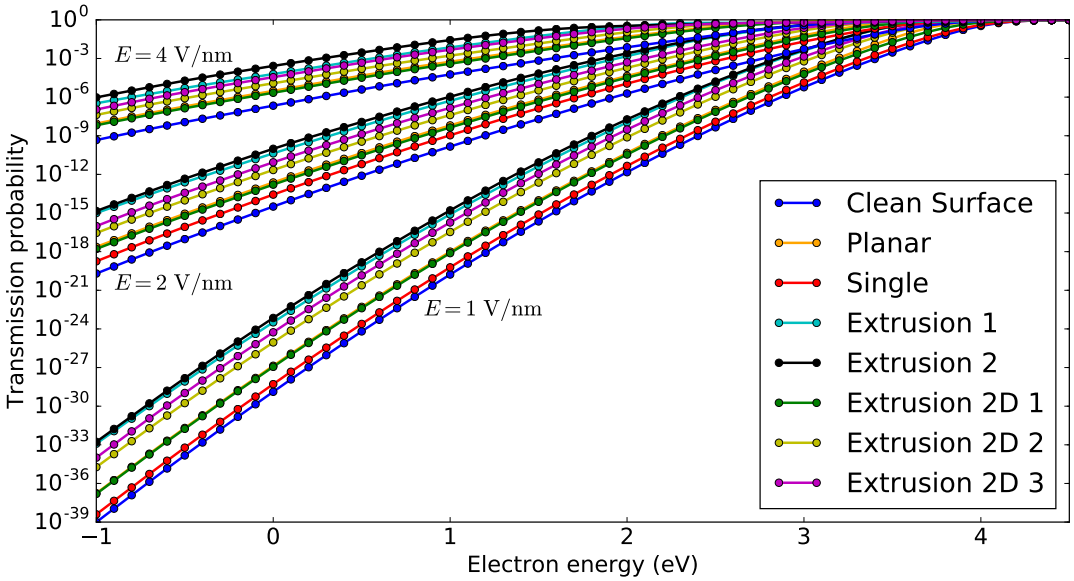

Figure 4.9: Transmission probability dependence on electron energy for all geometries and electric fields. Markers show calculated data points. The energy on x axis is given with respect to Fermi level. Data for Single adatom with electric field 4 V/nm is missing, as the DFT calculation did not finish in time.

Geometry	ϕ_0	ϕ_1	ϕ_2	ϕ_4
Clean	4.84	4.84	4.84	4.84
Planar	4.50	4.63	4.45	4.38
Single	4.69	4.78	4.65	–
Ext 1	4.26	4.26	3.96	3.83
Ext 2	4.28	4.22	3.88	3.53
Ext 2D 1	4.57	4.64	4.49	4.44
Ext 2D 2	4.42	4.43	4.24	4.14
Ext 2D 3	4.38	4.35	4.12	3.93

Table 4.3: Work function results: ϕ_0 corresponds to no electric field, obtained from the conventional analysis (Table 4.2), ϕ_1 corresponds to 1 V/nm, ϕ_2 to 2 V/nm and ϕ_4 to 4 V/nm. All values are given in eV. The data for cases with electric field was obtained from the quantum transport results.

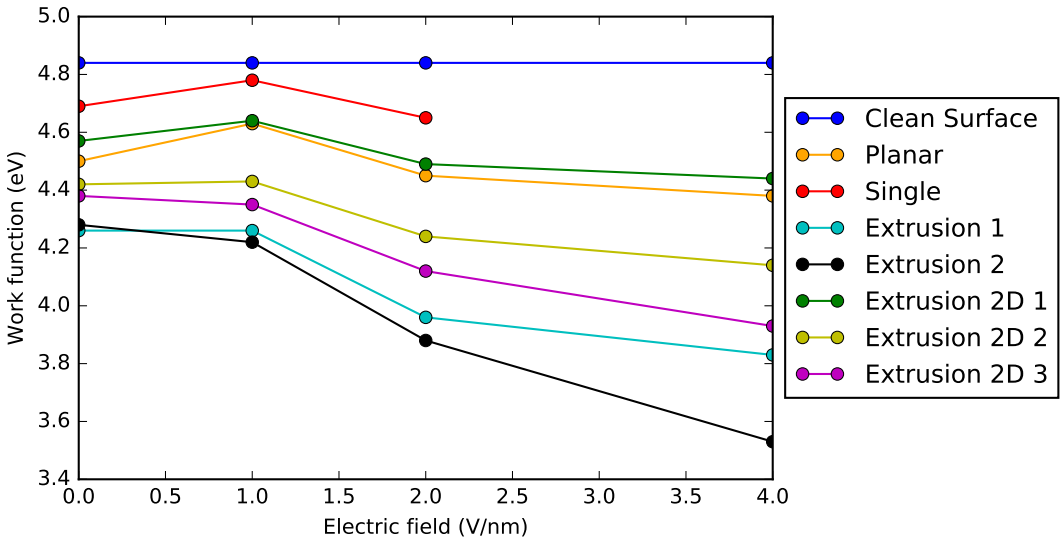

Figure 4.10: Work function results. Data from Table 4.3 visualized.

5 Conclusions

As a result of this work, the mathematical model for describing the electrical and thermal behaviour of surface defects was improved with the addition of the Nottingham effect and more accurate emission current calculations. The methodology for efficient evaluations of direct integrals for the Nottingham effect and the emission currents was developed and implemented. Additionally, a high-performance finite element code was developed based on the mathematical model, which can conveniently be interfaced and used together with atomic scale simulation software, such as molecular dynamics or kinetic Monte Carlo implementations.

Finite element analysis of the electrical and thermal behaviour of multiple different emitters with varying work functions from 3.0 to 4.5 eV, and varying geometries in the length scales $10 \ldots 100$ nm were conducted. The work function variation was validated by density functional theory calculations. The results from the finite element simulations showed that for the geometrical defects, where the base of the protrusion gets larger at the bottom, the Nottingham heating effect dominates over ohmic heating. The electric field, which causes the emitters to melt was reduced by up to 27% by taking Nottingham effect into account. However, if the heat conduction is hampered between the surface defect and the bulk metal, Nottingham effect might even start to cool the surface, but this would not significantly affect the electric field value when the defect melts.

The finite element simulations also revealed a possible collective effect of multiple different field emitters, which would introduce a deviation from the straight Fowler-Nordheim plot. As the emitters start to melt, the role of the dominating emitter, which determines the slope of the Fowler-Nordheim plot, continually shifts to different emitters. This phenomenon can increase the apparent field enhancement factor arbitrarily.

Density functional theory calculations were performed to investigate the work function changes for surfaces with different kinds of atomistic scale surface defects. Conventional analysis, without taking electric field into account, showed that considerable decrease of work function with respect to the clean (111) surface can occur. The largest lowering with respect to the (111) clean surface value of 4.84 eV was by 0.58 eV.

Methodology for assessing work function dependence on the electric field was developed. The main idea behind this methodology is to determine the work function from the dependence of electron transmission probability on its energy. The surface barrier was obtained from density functional theory calculations and the transmission probability dependence on energy was found with tight-binding quantum transport calculations. This methodology was applied to the studied atomic scale surface defects. The dependence of work function on electric field was significant for all the surface defects. The largest work function reduction with respect to the clean (111) surface for the electric field of 1 GV/m was 0.62 eV, for 2 GV/m was 0.96 eV and for 4 GV/m was 1.31 eV.

Acknowledgements

First of all, I would like to deeply thank my supervisor Vahur Zadin for all the guidance and interesting discussions throughout the years. Secondly, I am very grateful to Artur Tamm, who introduced me to the interesting and mysterious world of density functional theory. I am also thankful for having had the pleasure of sharing an office with Kristian Kuppart, Simon Vigonski, Robert Aare and Priit Priimägi, with whom I had countless engaging discussions. Some of the discussions were even related to work.

I would like to thank the whole friendly collective at the Intelligent Materials and Systems lab and the head of the lab, Prof. Alvo Aabloo, for providing me with an excellent work and study environment. Additionally, I would like to thank everyone at the Materials for Accelerator Technology work group at the Helsinki University, especially Mihkel Veske for fruitful collaborations. I am also very grateful to the High Performance Computing Center of the University of Tartu for allowing me to use their computing facilities.

And last but not least, I express my deepest gratitude towards all family and friends who have supported me throughout my studies.

References

[1] M Aicheler et al. *A Multi-TeV Linear Collider Based on CLIC Technology: CLIC Conceptual Design Report*. Tech. rep. CERN-2012-007. SLAC-R-985. KEK-Report-2012-1. PSI-12-01. JAI-2012-001. Geneva, 2012. URL: https://cds.cern.ch/record/1500095.

[2] M J Boland et al. *Updated baseline for a staged Compact Linear Collider*. Tech. rep. arXiv:1608.07537. CERN-2016-004. Geneva, Aug. 2016. URL: https://cds.cern.ch/record/2210892.

[3] Walter Wuensch. *Advances in the Understanding of the Physical Processes of Vacuum Breakdown*. Tech. rep. CERN-OPEN-2014-028. CLIC-Note-1025. Geneva: CERN, May 2013. URL: https://cds.cern.ch/record/1694664.

[4] M. Kildemo, S. Calatroni, and M. Taborelli. "Breakdown and field emission conditioning of Cu, Mo, and W". In: *Physical Review Special Topics - Accelerators and Beams* 7.9 (Sept. 2004), p. 092003. ISSN: 1098-4402. DOI: 10.1103/PhysRevSTAB.7.092003.

[5] G. A. Mesyats and D. I. Proskurovsky. *Pulsed Electrical Discharge in Vacuum*. Springer-Verlag, 1989, p. 293. ISBN: 0387507256.

[6] C.Z. Antoine, F. Peauger, and F. Le Pimpec. "Erratum to: Electromigration occurences and its effects on metallic surfaces submitted to high electromagnetic field: A novel approach to breakdown in accelerators". In: *Nuclear Instruments and Methods in Physics Research Section A: Accelerators, Spectrometers, Detectors and Associated Equipment* 670 (Apr. 2012), pp. 79–94. ISSN: 01689002. DOI: 10.1016/j.nima.2012.01.027.

[7] J Paulini, T Klein, and G Simon. "Thermo-field emission and the Nottingham effect". In: *Journal of Physics D: Applied Physics* 26.8 (Aug. 1993), pp. 1310–1315. ISSN: 0022-3727. DOI: 10.1088/0022-3727/26/8/024.

[8] K L Jensen et al. "Electron emission contributions to dark current and its relation to microscopic field enhancement and heating in accelerator structures". In: *Physical Review Special Topics-Accelerators and Beams* 11.8 (2008), p. 81001.

[9] A C Keser et al. "Heating of Micro-protrusions in Accelerating Structures". In: (May 2013), p. 8. arXiv: 1305.3643. URL: http://arxiv.org/abs/1305.3643.

[10] Zeke Insepov and Jim Norem. "Can surface cracks and unipolar arcs explain breakdown and gradient limits?" In: *Journal of Vacuum Science & Technology A: Vacuum, Surfaces, and Films* 31.1 (Jan. 2013), p. 011302. ISSN: 0734-2101. DOI: 10.1116/1.4766929.

[11] A. Descoeudres et al. "Investigation of the dc vacuum breakdown mechanism". In: *Physical Review Special Topics - Accelerators and Beams* 12.9 (Sept. 2009), p. 092001. ISSN: 1098-4402. DOI: 10.1103/PhysRevSTAB.12.092001.

[12] Morten Kildemo. "New spark-test device for material characterization". In: *Nuclear Instruments and Methods in Physics Research Section A: Accelerators, Spectrometers, Detectors and Associated Equipment* 530.3 (2004), pp. 596–606. ISSN: 01689002. DOI: 10.1016/j.nima.2004.04.230.

[13] R H Fowler and L Nordheim. "Electron Emission in Intense Electric Fields". In: *Proceedings of the Royal Society of London. Series A* 119.781 (1928), pp. 173–181. DOI: 10.1098/rspa.1928.0091.

[14] E L Murphy and R H Good. "Thermionic Emission, Field Emission, and the Transition Region". In: *Phys. Rev.* 102.6 (June 1956), pp. 1464–1473. DOI: 10.1103/PhysRev.102.1464.

[15] H. J. Qian et al. "Experimental investigation of thermal emittance components of copper photocathode". In: *Physical Review Special Topics - Accelerators and Beams* 15.4 (Apr. 2012), p. 040102. ISSN: 1098-4402. DOI: 10.1103/PhysRevSTAB.15.040102.

[16] J. F. Jia et al. "Variation of the local work function at steps on metal surfaces studied with STM". In: *Physical Review B* 58.3 (July 1998), pp. 1193–1196. ISSN: 0163-1829. DOI: 10.1103/PhysRevB.58.1193.

[17] Flyura Djurabekova et al. "Local changes of work function near rough features on Cu surfaces operated under high external electric field". In: *Journal of Applied Physics* 114.24 (Dec. 2013), p. 243302. ISSN: 0021-8979. DOI: 10.1063/1.4856875.

[18] Neil W. Ashcroft and N. David Mermin. *Solid state physics*. Saunders College, 1976, p. 826. ISBN: 0030493463.

[19] A. Modinos. *Field, Thermionic, and Secondary Electron Emission Spectroscopy*. Boston, MA: Springer US, 1984. ISBN: 978-1-4757-1450-0. DOI: 10.1007/978-1-4757-1448-7.

[20] K L Jensen. *Electron Emission Physics*. Vol. 149. Advances in Imaging and Electron Physics. Elsevier, 2007, pp. 47–146. ISBN: 9780123742070. DOI: 10.1016/S1076-5670(07)49002-4.

[21] Richard G Forbes. "Use of energy-space diagrams in free-electron models of field electron emission". In: *Surface and interface analysis* 36.5-6 (2004), pp. 395–401.

[22] A. Kiejna and Kazimierz Wojciechowski. *Metal surface electron physics*. Elsevier Science Ltd., 1996, p. 303. ISBN: 9780080536347.

[23] David J. Griffiths. *Introduction to Quantum Mechanics*. Pearson, 2013, p. 428. ISBN: 1292024089.

[24] S. Miller and R. Good. "A WKB-Type Approximation to the Schrödinger Equation". In: *Physical Review* 91.1 (July 1953), pp. 174–179. ISSN: 0031-899X. DOI: 10.1103/PhysRev.91.174.

[25] Richard G Forbes. "Simple good approximations for the special elliptic functions in standard Fowler-Nordheim tunneling theory for a Schottky-Nordheim barrier". In: *Applied physics letters* 89.11 (2006), p. 113122.

[26] Sylvain Coulombe and Jean-Luc Meunier. "A comparison of electron-emission equations used in arc - cathode interaction calculations". In: *Journal of Physics D: Applied Physics* 30.20 (Oct. 1997), pp. 2905–2910. ISSN: 0022-3727. DOI: 10.1088/0022-3727/30/20/019.

[27] E. Hantzsche. "The Thermo-Field Emission of Electrons in Arc Discharges". In: *Beiträge aus der Plasmaphysik* 22.4 (1982), pp. 325–346. ISSN: 00058025. DOI: 10.1002/ctpp.19820220403.

[28] Richard G. Forbes and Jonathan H.B. Deane. "Reformulation of the standard theory of Fowler–Nordheim tunnelling and cold field electron emission". In: *Proceedings of the Royal Society A: Mathematical, Physical and Engineering Sciences* 463.2087 (Nov. 2007), pp. 2907–2927. ISSN: 1364-5021. DOI: 10.1098/rspa.2007.0030.

[29] S D Liang. *Quantum Tunneling and Field Electron Emission Theories*. World Scientific Publishing Company, 2013. ISBN: 9789814440233.

[30] Michael K. Miller and Richard G. Forbes. *Atom-Probe Tomography*. Boston, MA: Springer US, 2014. ISBN: 978-1-4899-7429-7. DOI: 10.1007/978-1-4899-7430-3.

[31] Shigehiko Yamamoto. "Fundamental physics of vacuum electron sources". In: *Reports on Progress in Physics* 69.1 (Jan. 2006), pp. 181–232. ISSN: 0034-4885. DOI: 10.1088/0034-4885/69/1/R04.

[32] R. Smoluchowski. "Anisotropy of the Electronic Work Function of Metals". In: *Physical Review* 60.9 (Nov. 1941), pp. 661–674. ISSN: 0031-899X. DOI: 10.1103/PhysRev.60.661.

[33] K. Jakobi. "3.1.2.4 Work function data". In: *Electronic and Vibrational Properties*. Berlin/Heidelberg: Springer-Verlag, 1994, pp. 56–68. DOI: 10.1007/10086058_16.

[34] P A Chatterton. "A theoretical study of field emission initiated vacuum breakdown". en. In: *Proceedings of the Physical Society* 88.1 (May 1966), pp. 231–245. ISSN: 0370-1328. DOI: 10.1088/0370-1328/88/1/326.

[35] S. Sun and L. K. Ang. "Analysis of nonuniform field emission from a sharp tip emitter of Lorentzian or hyperboloid shape". In: *Journal of Applied Physics* 113.14 (Apr. 2013), p. 144902. ISSN: 00218979. DOI: 10.1063/1.4798926.

[36] Olek C Zienkiewicz, Robert L Taylor, and J.Z. Zhu. *The Finite Element Method: Its Basis and Fundamentals*. Butterworth-Heinemann, 2005, p. 752. ISBN: 008047277X.

[37] Christian Grossmann and Hans-Görg Roos. *Numerical Treatment of Partial Differential Equations*. Springer Science and Business Media, 2007, p. 591. ISBN: 3540715827.

[38] G.R. Liu and S. S. Quek. *The Finite Element Method: A Practical Course*. Elsevier Science, 2013, p. 464. ISBN: 0080994415.

[39] Richard M. Martin. *Electronic structure : basic theory and practical methods*. Cambridge University Press, 2004, p. 624. ISBN: 0521534402.

[40] M Born and R Oppenheimer. "Zur Quantentheorie der Molekeln". In: *Annalen der Physik* 389.20 (1927), pp. 457–484. ISSN: 1521-3889. DOI: 10.1002/andp.19273892002.

[41] P. Hohenberg and W. Kohn. "Inhomogeneous Electron Gas". In: *Physical Review* 136.3B (Nov. 1964), B864–B871. ISSN: 0031-899X. DOI: 10.1103/PhysRev.136.B864.

[42] W. Kohn and L. J. Sham. "Self-Consistent Equations Including Exchange and Correlation Effects". In: *Physical Review* 140.4A (Nov. 1965), A1133–A1138. ISSN: 0031-899X. DOI: 10.1103/PhysRev.140.A1133.

[43] Christoph W Groth et al. “Kwant: A software package for quantum transport”. In: *New Journal of Physics* 16.6 (June 2014), p. 063065. ISSN: 13672630. DOI: 10.1088/1367-2630/16/6/063065. arXiv: 1309.2926.

[44] Supriyo Datta. *Electronic Transport in Mesoscopic Systems*. Cambridge: Cambridge University Press, 1995. ISBN: 9780521599436. DOI: DOI:10.1017/CBO9780511805776.

[45] Stefan Parviainen et al. “Electronic processes in molecular dynamics simulations of nanoscale metal tips under electric fields”. In: *Computational Materials Science* 50.7 (May 2011), pp. 2075–2079. ISSN: 09270256. DOI: 10.1016/j.commatsci.2011.02.010.

[46] F. Djurabekova et al. “Atomistic modeling of metal surfaces under electric fields: Direct coupling of electric fields to a molecular dynamics algorithm”. In: *Physical Review E* 83.2 (Feb. 2011), p. 026704. ISSN: 1539-3755. DOI: 10.1103/PhysRevE.83.026704.

[47] Richard Allen Matula. “Electrical resistivity of copper, gold, palladium, and silver”. In: *Journal of Physical and Chemical Reference Data* 8 (1979), p. 1147.

[48] Constance E Schuster, Mark G Vangel, and HA Schafft. “Improved estimation of the resistivity of pure copper and electrical determination of thin copper film dimensions”. In: *Microelectronics Reliability* 41.2 (2001), pp. 239–252.

[49] Roger J. Elliott and Alan F. Gibson. *An Introduction to Solid State Physics and Its Applications*. Macmillan, 1974, p. 490. ISBN: 0333110234.

[50] Prem Nath and K.L. Chopra. “Thermal conductivity of copper films”. In: *Thin Solid Films* 20.1 (Jan. 1974), pp. 53–62. ISSN: 00406090. DOI: 10.1016/0040-6090(74)90033-9.

[51] Zhuomin Zhang. *Nano/Microscale Heat Transfer*. McGraw Hill Professional, 2007, p. 479. ISBN: 0071509739.

[52] AE Yarimbiyik et al. “Experimental and simulation studies of resistivity in nanoscale copper films”. In: *Microelectronics Reliability* 49.2 (Feb. 2009), pp. 127–134. ISSN: 00262714. DOI: 10.1016/j.microrel.2008.11.003.

[53] E. H. Sondheimer. “The mean free path of electrons in metals”. In: *Advances in Physics* 50.6 (Sept. 2001), pp. 499–537. ISSN: 0001-8732. DOI: 10.1080/00018730110102187.

[54] H. H. Mende and G. Thummes. “Surface scattering of electrons on copper whiskers and its influence on the electrical resistivity at 4.2 K”. In: *Applied Physics* 6.1 (Feb. 1975), pp. 93–97. ISSN: 0340-3793. DOI: 10.1007/BF00883555.

[55] *Multiphysics Modeling and Simulation Software - COMSOL*. 2013. URL: http://www.comsol.com/.

[56] *COMSOL Multiphysics 5.0 User’s Guide*. 2014.

[57] M Veske. *Finite Elements on Crystal Surfaces*. 2017. URL: https://github.com/veskem/femocs.

[58] W Bangerth, R Hartmann, and G Kanschat. “deal.II — A General-Purpose Object-Oriented Finite Element Library”. In: *ACM Transactions on Mathematical Software* 33.4 (2007), pp. 1–27. ISSN: 00983500. DOI: 10.1145/1268776.1268779.

[59] G. Kresse and J. Furthmüller. “Efficient iterative schemes for ab initio total-energy calculations using a plane-wave basis set”. In: *Physical Review B* 54.16 (Oct. 1996), pp. 11169–11186. DOI: 10.1103/PhysRevB.54.11169.

[60] G. Kresse and J. Furthmüller. “Efficiency of ab-initio total energy calculations for metals and semiconductors using a plane-wave basis set”. In: *Computational Materials Science* 6.1 (July 1996), pp. 15–50. ISSN: 09270256. DOI: 10.1016/0927-0256(96)00008-0.

[61] John P. Perdew, Kieron Burke, and Matthias Ernzerhof. “Generalized Gradient Approximation Made Simple”. In: *Physical Review Letters* 77.18 (Oct. 1996), pp. 3865–3868. ISSN: 0031-9007. DOI: 10.1103/PhysRevLett.77.3865.

[62] K Eimre. *Field, currents, heating finite element code*. 2017. URL: https://github.com/eimrek/dealii-field-currents-heating.

[63] J. Sun and S.L. Simon. “The melting behavior of aluminum nanoparticles”. In: *Thermochimica Acta* 463.1 (2007), pp. 32–40. ISSN: 00406031. DOI: 10.1016/j.tca.2007.07.007.

[64] W.H. Qi and M.P. Wang. “Size and shape dependent melting temperature of metallic nanoparticles”. In: *Materials Chemistry and Physics* 88.2 (2004), pp. 280–284. ISSN: 02540584. DOI: 10.1016/j.matchemphys.2004.04.026.

A Supply function derivation

The expression for the number of states which cross a unit area (without losing generality, the area is assumed to be normal to x direction), per unit time, with total energy between 0 and E and normal (to the area) energy defined by $E_x = \frac{\hbar^2 k_x^2}{2m}$ between 0 and E_x is given by (2.7). To evaluate the integral

$$\int\limits_{(E,E_x)} v_x d\boldsymbol{k}, \tag{A.1}$$

the limits will be first set to $(0, E_x)$, $(0, E)$ and the differentiated to obtain the needed result. The calculation is the following

$$\begin{aligned}\int\int\int v_x dk'_y dk'_z dk'_x = \int\limits_0^{\sqrt{\frac{2mE_x}{\hbar^2}}} v_x \left(\int\int dk'_y dk'_z\right) dk'_x = \ldots \\ \ldots = \int\limits_0^{\sqrt{\frac{2mE_x}{\hbar^2}}} v_x \left(\int\limits_0^{2\pi} \int\limits_0^{\sqrt{\frac{2mE}{\hbar^2} - k_x^2}} k' dk' d\theta\right) dk'_x = \frac{\pi m}{\hbar^3}(2EE_x - E_x^2).\end{aligned} \tag{A.2}$$

Differentiating this result with respect to E and E_x, we obtain

$$\int\limits_{(E,E_x)} v_x d\boldsymbol{k} = \frac{2\pi m}{\hbar^3} dE dE_x \tag{A.3}$$

and the supply function defined by (2.7) is given by

$$N(E, E_x) dE dE_x = \frac{m}{2\pi^2 \hbar^3} f_{\mathrm{FD}}(E) dE dE_x. \tag{A.4}$$

B Weak formulation for Newton's iteration

The non-linear problem that arises from the electric current (3.5) and heat (3.9) partial differential equations is the following

$$\begin{aligned} \nabla \cdot \sigma(T)\nabla\varphi &= 0 && \text{in } \Omega \\ \nabla \cdot \kappa(T)\nabla T &= -\sigma(T)(\nabla\varphi)^2 && \text{in } \Omega \\ \vec{n} \cdot (\sigma(T)\nabla\varphi) &= J(T) && \text{on } \delta\Omega_1 \\ \vec{n} \cdot (\kappa(T)\nabla T) &= Q(T) && \text{on } \delta\Omega_1 \\ \varphi &= 0 && \text{on } \delta\Omega_2 \\ T &= 300 && \text{on } \delta\Omega_2, \end{aligned} \tag{B.1}$$

where φ is the electric potential, T is temperature, σ and κ are electrical and thermal conductivities. Domain Ω describes the whole copper domain, boundary $\delta\Omega_1$ is the copper-vacuum boundary and $\delta\Omega_2$ is the boundary corresponding to the bulk copper. See Figure 3.1 for further details. $J(T)$ and $Q(T)$ describe the non-linear Neumann boundary conditions corresponding to emission currents and Nottingham heat flux. The thermal and electrical isolation boundary conditions on the sides are so-called natural boundary conditions and are taken into account implicitly.

Iterating scheme for Newton's method can be formulated as

$$\begin{aligned} R'(U_k)\delta U_k &= -R(U_k), \\ U_{k+1} &= U_k + \delta U_k \end{aligned} \tag{B.2}$$

where U_k is the k-th iteration solution vector and $R(U_k)$ is the residual and δU_k is the step, for which the linear system is solved in each iteration.

In the case of current problem, by using variational calculus,

$$R(U_k) = \begin{bmatrix} \nabla \cdot \sigma \nabla \varphi_k \\ \sigma(\nabla\varphi_k)^2 + \nabla \cdot \kappa \nabla T_k \end{bmatrix} \tag{B.3}$$

$$R'(U_k)\delta U_k = \begin{bmatrix} \nabla \cdot \sigma \nabla \delta\varphi_k + \nabla \cdot \left(\frac{d\sigma}{dT}(\nabla\varphi_k)\delta T_k\right) \\ 2\sigma(\nabla\varphi_k)(\nabla\delta\varphi_k) + \frac{d\sigma}{dT}(\nabla\varphi_k)^2\delta T_k + \nabla \cdot \left(\frac{d\kappa}{dT}(\nabla T_k)\delta T_k + \kappa\nabla\delta T_k\right) \end{bmatrix}. \tag{B.4}$$

The weak formulation is

$$\int_\Omega \begin{bmatrix} \phi_i & \psi_i \end{bmatrix} R'(U_k)\delta U_k = -\int_\Omega \begin{bmatrix} \phi_i & \psi_i \end{bmatrix} R(U_k), \tag{B.5}$$

where ϕ_i and ψ_i are the shape functions of electric potential and temperature. Using the notation of $(f,g) \equiv \int_\Omega fgdV$ and expressing all terms explicitly on both sides, we obtain

$$\begin{aligned}
\int_\Omega \begin{bmatrix}\phi_i & \psi_i\end{bmatrix} R'(U_k)\delta U_k = &(\phi_\varphi, \nabla\cdot\sigma\nabla\delta\varphi_k) \\
&+ \left(\phi_\varphi, \nabla\cdot\left(\tfrac{d\sigma}{dT}(\nabla\varphi_k)\delta T_k\right)\right) \\
&+ (\phi_T, 2\sigma(\nabla\varphi_k)(\nabla\delta\varphi_k)) \\
&+ \left(\phi_T, \tfrac{d\sigma}{dT}(\nabla\varphi_k)^2\delta T_k\right) \\
&+ \left(\phi_T, \nabla\cdot\left(\tfrac{d\kappa}{dT}(\nabla T_k)\delta T_k + \kappa\nabla\delta T_k\right)\right) \\
= &-(\nabla\phi_\varphi, \sigma\nabla\delta\varphi_k) + \int_{\delta\Omega}\phi_\varphi\vec{n}\cdot(\sigma\nabla\delta\varphi_k) \\
&-\left(\nabla\phi_\varphi, \left(\tfrac{d\sigma}{dT}(\nabla\varphi_k)\delta T_k\right)\right) + \int_{\delta\Omega}\phi_\varphi\vec{n}\cdot\left(\tfrac{d\sigma}{dT}(\nabla\varphi_k)\delta T_k\right) \\
&+ (\phi_T, 2\sigma(\nabla\varphi_k)(\nabla\delta\varphi_k)) \\
&+ \left(\phi_T, \tfrac{d\sigma}{dT}(\nabla\varphi_k)^2\delta T_k\right) \\
&-\left(\nabla\phi_T, \left(\tfrac{d\kappa}{dT}(\nabla T_k)\delta T_k + \kappa\nabla\delta T_k\right)\right) \\
&+ \int_{\delta\Omega}\phi_T\vec{n}\cdot\left(\tfrac{d\kappa}{dT}(\nabla T_k)\delta T_k + \kappa\nabla\delta T_k\right)
\end{aligned} \tag{B.6}$$

$$\begin{aligned}
-\int_\Omega \begin{bmatrix}\phi_\varphi & \phi_T\end{bmatrix} R(U_k) = &-(\phi_\varphi, \nabla\cdot\sigma\nabla\varphi_k) \\
&-\left(\phi_T, \sigma(\nabla\varphi_k)^2\right) \\
&-(\phi_T, \nabla\cdot\kappa\nabla T_k) \\
= &(\nabla\phi_\varphi, \sigma\nabla\varphi_k) - \int_{\delta\Omega}\phi_\varphi\vec{n}\cdot\sigma\nabla\varphi_k \\
&-\left(\phi_T, \sigma(\nabla\varphi_k)^2\right) \\
&+(\nabla\phi_T, \kappa\nabla T_k) - \int_{\delta\Omega}\phi_T\vec{n}\cdot\kappa\nabla T_k.
\end{aligned} \tag{B.7}$$

After expressing the unknown functions $\delta\varphi_k$ and δT_k as linear combinations of the shape functions ϕ_φ and ϕ_T, the linear system of equations for one Newton's iteration is obtained. All of the integrals can be evaluated based on the boundary conditions. Both the Dirichlet and Neumann boundary conditions for $\delta\varphi$ and δT should be the same as for φ and T on the first iteration step and zero afterwards.

Non-exclusive licence to reproduce thesis and make thesis public

I, Kristjan Eimre

1. herewith grant the University of Tartu a free permit (non-exclusive licence) to:
   a) reproduce, for the purpose of preservation and making available to the public, including for addition to the DSpace digital archives until expiry of the term of validity of the copyright, and
   b) make available to the public via the web environment of the University of Tartu, including via the DSpace digital archives, as of 29.05.2020 until expiry of the term of validity of the copyright,

   Multiscale electrical and thermal simulations of metal surface defects in high electric field,

   supervised by Vahur Zadin,
2. I am aware of the fact that the author retains these rights.
3. I certify that granting the non-exclusive licence does not infringe the intellectual property rights or rights arising from the Personal Data Protection Act.

Tartu, May 28, 2017